Constraints on VHE gamma-ray emission of flat spectrum radio quasars with the MAGIC telescopes

S. Abe,[1] J. Abhir,[2] A. Abhishek,[3] V. A. Acciari,[4] A. Aguasca-Cabot,[5] I. Agudo,[6] T. Aniello,[7]
S. Ansoldi,[8]† L. A. Antonelli,[7] A. Arbet Engels,[9] C. Arcaro,[10] M. Artero,[4] K. Asano,[1] A. Babić,[11]
A. Baquero,[12] U. Barres de Almeida,[13] J. A. Barrio,[12] I. Batković,[10] A. Bautista,[9] J. Baxter,[1]
J. Becerra González,[14] W. Bednarek,[15] E. Bernardini,[10] J. Bernete,[16] A. Berti,[9] J. Besenrieder,[9]
C. Bigongiari,[7] A. Biland,[2] O. Blanch,[4] G. Bonnoli,[7] Ž. Bošnjak,[11] E. Bronzini,[7] I. Burelli,[8] G. Busetto,[10]
A. Campoy-Ordaz,[17] A. Carosi,[7] R. Carosi,[18] M. Carretero-Castrillo,[5] A. J. Castro-Tirado,[6] D. Cerasole,[19]
G. Ceribella,[9] Y. Chai,[1] A. Cifuentes,[16] E. Colombo,[4] J. L. Contreras,[12] J. Cortina,[16] S. Covino,[7]
G. D'Amico,[20] F. D'Ammando,[21] V. D'Elia,[7] P. Da Vela,[7] F. Dazzi,[7] A. De Angelis,[10] B. De Lotto,[8]
R. de Menezes,[22] A. Del Popolo,[23] M. Delfino,[4]‡ J. Delgado,[4]‡ C. Delgado Mendez,[16] F. Di Pierro,[22]
R. Di Tria,[19] L. Di Venere,[19] D. Dominis Prester,[24] A. Donini,[7] D. Dorner,[25] M. Doro,[10] D. Elsaesser,[26]
G. Emery,[27] J. Escudero,[6] L. Fariña,[4] A. Fattorini,[26] L. Foffano,[7] L. Font,[17] S. Fröse,[26] S. Fukami,[2]
Y. Fukazawa,[28] R. J. García López,[14] M. Garczarczyk,[29] S. Gasparyan,[30] M. Gaug,[17]
J. G. Giesbrecht Paiva,[13] N. Giglietto,[19] F. Giordano,[19] P. Gliwny ![ORCID],[15]★ N. Godinović,[31] T. Gradetzke,[26]
R. Grau,[4] D. Green,[9] J. G. Green,[9] P. Günther,[25] D. Hadasch,[1] A. Hahn,[9] T. Hassan,[16] L. Heckmann,[9]
J. Herrera,[14] D. Hrupec,[32] M. Hütten,[1] R. Imazawa,[28] K. Ishio,[15] I. Jiménez Martínez,[9] J. Jormanainen,[33]
T. Kayanoki,[28] D. Kerszberg,[4] Y. Kobayashi,[1] P. M. Kouch,[33] H. Kubo,[1] J. Kushida,[34] M. Láinez,[12]
A. Lamastra,[7] F. Leone,[7] E. Lindfors,[33] L. Linhoff,[26] S. Lombardi,[7] F. Longo,[8]§ R. López-Coto,[6]
M. López-Moya,[12] A. López-Oramas,[14] S. Loporchio,[19] A. Lorini,[3] E. Lyard,[27]
B. Machado de Oliveira Fraga,[13] P. Majumdar,[35] M. Makariev,[36] G. Maneva,[36] N. Mang,[26]
M. Manganaro,[24] S. Mangano,[16] K. Mannheim,[25] M. Mariotti,[10] M. Martínez,[4] M. Martínez-Chicharro,[16]
A. Mas-Aguilar,[12] D. Mazin,[1,37] S. Menchiari,[3] S. Mender,[26] D. Miceli,[10] T. Miener,[12] J. M. Miranda,[3]
R. Mirzoyan,[9] M. Molero González,[14] E. Molina,[14] H. A. Mondal,[35]★ A. Moralejo,[4] D. Morcuende,[6]
T. Nakamori,[38] C. Nanci,[7] V. Neustroev,[39] L. Nickel,[26] M. Nievas Rosillo,[14] C. Nigro,[4] L. Nikolić,[3]
K. Nilsson,[33] K. Nishijima,[34] T. Njoh Ekoume,[4] K. Noda,[40] S. Nozaki,[9] Y. Ohtani,[1] A. Okumura,[41]
J. Otero-Santos,[6] S. Paiano,[7] M. Palatiello,[8] D. Paneque,[9] R. Paoletti,[3] J. M. Paredes,[5] M. Peresano,[9]
M. Persic,[8]‖ M. Pihet,[10] G. Pirola,[9] F. Podobnik,[3] P. G. Prada Moroni,[18] E. Prandini,[10] G. Principe ![ORCID],[8]★¶
C. Priyadarshi,[4] W. Rhode,[26] M. Ribó,[5] J. Rico,[4] C. Righi,[7] N. Sahakyan,[30] T. Saito,[1] K. Satalecka,[33]
F. G. Saturni,[7] B. Schleicher,[25] K. Schmidt,[26] F. Schmuckermaier,[9] J. L. Schubert,[26] T. Schweizer,[9]
A. Sciaccaluga,[7] G. Silvestri,[10] J. Sitarek,[15] V. Sliusar,[27] D. Sobczynska,[15] A. Spolon,[10] A. Stamerra,[7]
J. Strišković,[32] D. Strom,[9] M. Strzys,[1] Y. Suda,[28] S. Suutarinen,[33] H. Tajima,[41] M. Takahashi,[41]
R. Takeishi,[1] P. Temnikov,[36] K. Terauchi,[42] T. Terzić,[24] M. Teshima,[1,9] S. Truzzi,[3] A. Tutone,[7] S. Ubach,[17]
J. van Scherpenberg,[9] M. Vazquez Acosta,[14] S. Ventura,[3] I. Viale,[10] C. F. Vigorito,[22] V. Vitale,[43] I. Vovk,[1]

★ E-mail: contact.magic@mpp.mpg.de
† Also at: International Center for Relativistic Astrophysics (ICRA), Rome, Italy.
‡ Also at: Port d'Informació Científica (PIC), E-08193 Bellaterra (Barcelona), Spain.
§ Also at: Dipartimento di Fisica, Università di Trieste, I-34127 Trieste, Italy.
‖ Also at: INAF Padova.
¶ Also at: Dipartimento di Fisica, Università di Trieste, I-34128 Trieste, Italy.

R. Walter,[27] M. Will,[9] C. Wunderlich,[3] T. Yamamoto,[44] N. Zywucka,[15]
V. F. Ramazani,[33] S. Buson[25] and S. Ciprini[43,45]

Affiliations are listed at the end of the paper

ABSTRACT

Flat spectrum radio quasars (FSRQs) constitute a class of jetted active galaxies characterized by a very luminous accretion disc, prominent and rapidly moving line-emitting cloud structures (broad-line region, BLR), and a surrounding dense dust structure known as dusty torus. The intense radiation field of the accretion disc strongly determines the observational properties of FSRQs. While hundreds of such sources have been detected at GeV energies, only a handful of them exhibit emission in the very-high-energy (VHE, $E \gtrsim 100$ GeV) range. This study presents the results and interpretation derived from a cumulative observation period of 174 h dedicated to nine FSRQs conducted with the Major Atmospheric Gamma-ray Imaging Cherenkov telescopes from 2008 to 2020. Our findings indicate no statistically significant ($\geq 5\sigma$) signal for any of the studied sources, resulting in upper limits on the emission within the VHE energy range. In two of the sources, we derived quite stringent constraints on the gamma-ray emission in the form of upper limits. Our analysis focuses on modelling the VHE emission of these two sources in search for hints of absorption signatures within the BLR radiation field. For these particular sources, constraints on the distance between the emission region and the central black hole are derived using a phenomenological model. Subsequently, these constraints are tested using a framework based on a leptonic model.

Key words: radiation mechanisms: non-thermal – quasars: emission lines – gamma-rays: galaxies.

1 INTRODUCTION

Active galactic nuclei (AGN) are one of the most luminous class of objects in our Universe. Jetted AGN whose jet is pointing towards or making a small angle with respect to the observer are called blazars. Based on their optical properties, blazars are divided into two groups: BL Lacertae (BL Lac) objects and flat spectrum radio quasars (FSRQs). Blazars with strong optical emission lines having an equivalent width (EW) of EW > 5 Å are classified as FSRQs, while those with weak or absent lines are referred to as BL Lacs (Urry & Padovani 1995). The distinction between FSRQ and BL Lac is unclear in some cases due to the lack of good quality measured optical spectra or changing EW of the lines during high states. Broad emission lines identifiable in the spectra of some AGNs are produced in the broad-line region (BLR), which is considered photoionized by thermal radiation from the accretion disc (Raiteri et al. 2007).

Two humps characterize the broad-band spectral energy distribution (SED) of blazars. The lower energy hump in the spectrum is caused by synchrotron emission produced by relativistic electrons within the jet. On the other hand, the higher energy component, typically peaking at GeV–TeV, is often interpreted as inverse Compton (IC) scattering. This scattering occurs between the relativistic electrons and either the synchrotron photons themselves (synchrotron self Compton, SSC) or external photons outside the jet (external Compton, EC). The SSC scenario is commonly used to explain the higher energy peak in BL Lac objects, while the EC scenario is favoured for FSRQs (Pacciani et al. 2014). The external photons are produced in the dusty torus (DT), in the BLR, or could come directly from the accretion disc (Dermer & Schlickeiser 2002; Böttcher 2007; Paliya et al. 2018; van den Berg et al. 2019). The nature of the dominating external radiation field depends on the location of the emission zone with respect to the black hole (BH). When the emission region is located within the BLR, a sharp cut-off in the gamma-ray spectrum is foreseen to occur due to the strong attenuation of

the high-energy (HE, order of a few GeV) and very-high-energy (VHE, $E \gtrsim 100$ GeV) gamma-rays through their interaction with the optical photons in the gamma–gamma pair production process. The opacity for HE photons could be very large, averting their escape from the emission region; therefore, if we can attribute the cause of the break/cut-off to the absorption, we can put a constraint on the location of the gamma-ray emitting zone (Sahakyan 2020).

Thus, the gamma-ray emission from FSRQs can be affected by internal absorption in the dense ultraviolet (UV)-optical photons of the BLR (Liu & Bai 2006; Costamante et al. 2018). Detection of gamma-rays from blazars by imaging atmospheric Cherenkov telescopes (IACTs) is also made difficult due to the interaction between VHE photons and lower energy extragalactic background light (EBL) photons (Finke, Razzaque & Dermer 2010; Domínguez et al. 2011; Saldana-Lopez et al. 2021; Finke et al. 2022), which also leads to electron-position pair creation. This process strongly attenuates VHE photons with energies above a characteristic energy, which depends on the redshift of the source, typically about 30 GeV for sources at redshift $z < 1$. The attenuation results in a softer spectrum observed on Earth than the intrinsic spectrum of extragalactic sources (Gerasimova, Nikishov & Rosenthal 1962), making the detection of distant sources challenging (see e.g. Aleksić et al. 2014).

The fourth catalogue of AGN detected by *Fermi* Large Area Telescope (LAT) (4LAC-DR3; Ajello et al. 2022) contains 2896 sources, among which 640 are FSRQs, and 1261 are BL Lacs. Based on the results from 4LAC, on average, FSRQs demonstrate softer spectra and stronger variability in the gamma-ray energy range than BL Lacs, confirming previous results (Dermer 2013). However, it is important to note that the stronger variability might be an observational bias due to the tendency of FSRQs to be brighter. The catalogues of hard *Fermi*-LAT sources (2FHL, Ackermann et al. 2016; 3FHL, Ajello et al. 2017) report detections of FSRQs at different energy thresholds; the number of FSRQs detected above 10 GeV in the 3FHL (integration time ~84 months) is 172, and the

number of FSRQs detected above 50 GeV in the 2FHL (integration time ∼80 months) is only 10.

FSRQs are generally located at higher cosmological distances than BL Lacs (Abdollahi et al. 2020), implying a strong absorption of gamma-rays by the EBL (see e.g. PKS 1441+25; Ahnen et al. 2015). The most distant (with redshift $z \sim 1$) AGNs ever detected in the VHE energy range are the FSRQ PKS 1441+25 at $z = 0.940$ (Ahnen et al. 2015), the FSRQ PKS 0346−27 at $z = 0.991$ (Angioni 2018; Wagner, Rani & H. E. S. S. Collaboration 2021) and the gravitationally lensed blazar QSO B0218+357 (Ahnen et al. 2016) at $z = 0.954$. At the end of 2023, the large-sized telescope prototype (LST-1) of the Cherenkov Telescope Array Observatory (CTAO) announced the detection of VHE emission from OP313 (Cortina & CTAO LST Collaboration 2023), an FSRQ located at redshift $z = 0.9997$, the farthest VHE source detected to date.

FSRQs are highly variable in the VHE band (see e.g. Meyer, Scargle & Blandford 2019). The VHE gamma-ray flux has been observed to fluctuate even by two orders of magnitude (Zacharias et al. 2019). Due to this, the most successful approach for studying the FSRQs in the VHE gamma-rays is to follow up alerts of enhanced activity at lower energies. However, it should be kept in mind that this strategy is only effective if the flare is of long duration and not on hour-time-scale. Additionally, continuous monitoring is necessary for this approach to be fruitful.

The first catalogue reporting upper limits (ULs) from FSRQs in the TeV energy range was carried out by the Whipple Collaboration (Falcone et al. 2004). A catalogue of ULs for AGNs, including FSRQs sources, was also published by the High Energy Stereoscopic System Collaboration (H. E. S. S.; Aharonian et al. 2008; H. E. S. S. Collaboration et al. 2014) and the very energetic radiation imaging telescope array system (VERITAS; Archambault et al. 2016). Nowadays, the VERITAS collaboration performs a systematic and unbiased search for the TeV emission from a set of FSRQs (Patel 2021).

The current list of detected blazars in the VHE band, available in *TeVCat*[1] (Wakely & Horan 2008), consist of 70 BL Lacs and only 9 FSRQs.

Observations of FSRQs in the VHE band may provide information about their nature and radiation processes. The longstanding question pertains to the location of the gamma-ray emitting region within FSRQs. Recent evidence suggests that this region is likely located beyond the BLR, at least during the epoch of VHE gamma-ray emission. Such evidence stems both from the absence of absorption in the *Fermi*-LAT observations of FSRQs – where 2/3 of the selected FSRQs in the study of Costamante et al. (2018) displayed no signs of absorption within the >100 GeV range, as well as from the detection of VHE gamma-ray emissions from FSRQs. FSRQs experience variability in VHE gamma-rays with time-scales as low as tens of minutes (see Aleksić et al. 2011b; Zacharias et al. 2021). It has been long argued that such variability would more naturally occur closer to the black hole; however, as it has become evident that jets have substructures and that the emission region does not have to fill the full jet diameter (see e.g. Hovatta & Lindfors 2019 for a recent review), this line of argumentation has become less popular. Nowadays, the understanding of VHE emission of FSRQs still needs to be completed.

In this paper, we present the VHE gamma-ray observations, data analysis, and results of nine FSRQs: TXS 0025+197, B2 0234+28, AO 0235+16, 4C+55.17, OP 313, CTA 102, B2 2234+28A, TXS

2241+406, and 3C 454.3. The data used in this study were gathered by the Major Atmospheric Gamma-ray Imaging Cherenkov telescopes (MAGIC) together with the optical data from the Kungliga Vetenskapsakademien (KVA) along with X-ray, UV, and optical data from *Swift*-X-ray Telescope (XRT) and *Swift*-Ultraviolet and Optical Telescope (UVOT), respectively. We also performed dedicated *Fermi*-LAT analysis contemporaneous to the MAGIC observations. Additionally, we used gamma-ray data collected by *Fermi*-LAT over 12 yr to compare these observations with an average state of the sources studied in this paper. We present here a MAGIC catalogue of ULs on the gamma-ray emission of these sources. Next, we construct a theoretical model using the *Fermi*-LAT data and the MAGIC ULs exploiting the absorption in BLR and, finally, derive a broad-band emission model based on the EC scenario.

The paper is organized in the following way: a description of instruments and data analysis method is included in Section 2, notes on the individual sources are reported in Section 3, gamma-ray emission results are discussed in Section 4, constraints on the distance between the emission region and the central black hole are described in Section 4.2, along with broad-band modelling. Finally, the results are summarized in Section 5. In the Appendix, we provide the light curves (LCs) for seven out of nine sources and SEDs for all the studied sources.

2 INSTRUMENTS, OBSERVATIONS, AND DATA ANALYSES

We investigate the broad-band emission of the sources by using data from the following instruments: MAGIC (VHE gamma-rays), *Fermi*-LAT (GeV gamma-rays), KVA (optical band) as well as, for selected sources, *Swift*-UVOT (UV and optical bands), and *Swift*-XRT (X-rays).

2.1 MAGIC

MAGIC is a stereoscopic system consisting of two 17-m diameter IACTs located at Observatorio del Roque de los Muchachos on the Canary Island of La Palma (Aleksić et al. 2016a). The first telescope, MAGIC I, was constructed between 2002 and 2003 and operated in standalone or *monoscopic* mode since 2004, with an energy threshold of 60 GeV at trigger level (Aleksić et al. 2011a). A second telescope, MAGIC II, was finished in 2008 and operates, since 2009, alongside the first telescope in *stereoscopic* mode. The MAGIC telescopes are able to reach a low-energy threshold of 50 GeV at low-zenith angles in stereo mode, which has been operational since 2009 (Aleksić et al. 2012, 2016b).

Due to such low-energy thresholds, they are well-suited for studies of high-redshift blazars. Some of the data used in this study were taken with a standard trigger, and the rest were taken with a special low-energy analogue trigger called Sum-Trigger-II, designed to improve the performance of the telescopes reaching an even lower energy threshold of ∼15 GeV (Dazzi et al. 2021). Sum-Trigger-II in a stereoscopic system allows the combination of the low-energy trigger threshold along with better background rejection compared to standard stereo trigger. It also requires a special analysis procedure to get a larger effective area at lower energies. At higher energies, SUM-Trigger-II has a smaller trigger region. Therefore, it is used only with selected low-energy sources, particularly those located at high redshifts. The observations were carried out in wobble mode (Fomin et al. 1994) with a 0.4° offset and four symmetric positions distributed around the camera centre, improving the statistical accuracy of background estimation. The

data selection was based on the atmospheric transmission measured mainly with light detection and ranging system (Schmuckermaier et al. 2023) and rates of background events. The data were analysed using the MAGIC Analysis Reconstruction Software framework (Zanin et al. 2013; Aleksić et al. 2016b). For each source, all of the data available, therefore also from the different observation periods and consequently flux states, were combined together to obtain a constraint on its VHE emission. The ULs were calculated using the method presented in Rolke, López & Conrad (2005), with a 95 per cent Confidence Level (C.L.). This approach assumes a systematic Gaussian uncertainty in the detector efficiency, i.e. the effective area, with a σ of 30 per cent.

2.2 *Fermi*-LAT

The Large Area Telescope onboard the *Fermi* satellite is a gamma-ray instrument that detects photons by conversion into electron–positron pairs and has an operational energy range from 20 MeV to more than 300 GeV. It comprises a high-resolution converter tracker (for direction measurement of the incident gamma-rays), a CsI(Tl) crystal calorimeter (for energy measurement), and an anticoincidence shield detector to identify and veto the background of charged particles (Atwood et al. 2009). We performed a dedicated analysis of the *Fermi*-LAT data for each of the nine MAGIC-observed FSRQs using 12 yr of LAT observations taken between 2008 August 4th and 2020 August 4th. Additionally, as we will describe later, for each of the sources we analysed the LAT data centred on the times of the MAGIC observations (see Appendix A for the exact times). A similar analysis technique has also been applied in Principe et al. (2021).

We selected P8R3 SOURCE class events (Bruel et al. 2018), in the energy range between 100 MeV and 1 TeV, in a region of interest (ROI) of 15° radius centred on the position of each selected source. The value of the low-energy threshold is motivated by the large uncertainties in the arrival directions of the photons below 100 MeV (Principe et al. 2018), leading to possible confusion between point-like sources and the Galactic diffuse component.

The analysis (which consists of model optimization, localization, spectrum, and variability study) was performed with FERMIPY[2] (version 1.0.1) (Wood et al. 2017), and the *Fermi* Science Tools (version 11-07-00). The count maps were created with a pixel size of 0.1°. All gamma-rays with zenith angle larger than 95° were excluded to limit the contamination from secondary gamma-rays from the Earth's limb (Abdo et al. 2009b). We made a harder cut at low energies by reducing the maximum zenith angle and by excluding event types with the worst point spread functions[3] (PSF). Namely, for energies below 300 MeV, we excluded events with a zenith angle larger than 85°, as well as photons from the PSF0 event type, while above 300 MeV we used all event types. The P8R3_SOURCE_V3 instrument response functions are used. The model used to describe the sky includes all point-like and extended LAT sources, located at a distance < 20° from each FSRQ position, listed in the Fourth *Fermi*-LAT Source Catalogue (4FGL-DR2; Abdollahi et al. 2020), as well as the Galactic diffuse and isotropic emission. For these two

latter contributions, we made use of the same templates[4] adopted to compile the 4FGL-DR2. For the analysis, we first optimized the model for the ROI, then we searched for the possible presence of new sources, and finally, we relocalized the source.

We investigated the possible presence of additional faint sources, not in 4FGL-DR2, by generating test statistic[5] (TS) maps. No new source (TS > 25) was detected in the vicinity of our targets. Moreover, we checked also if there was any variation using the recently release 4FGL-DR3 (Abdollahi et al. 2022), no significant variation is observed for the results of the selected sources. We left free to vary the diffuse background and the spectral parameters of the sources within 5° of our targets. For the sources at a distance between 5° and 10°, only the normalization was fitted, while we fixed the parameters of all the sources within the ROI at larger angular distances from our targets. The spectral fit was performed over the energy range from 100 MeV to 1 TeV. To study the variability of the gamma-ray emission of each FSRQ, we divided the *Fermi*-LAT data into time intervals of one week. For the light-curve analysis, we fixed the photon index to the value obtained for 12 yr and left only the normalization free to vary. The 95 per cent upper limit is reported for each time interval with TS < 10.

In addition to the study of the whole 12 yr of *Fermi*-LAT data, we performed a stacking analysis selecting and folding together all the photons observed in the considered periods, chosen to be simultaneous (around) to the MAGIC observations (for the exact time considered for the LAT analysis see Table A1 and Fig. A1 in the Appendix). In particular, for each source we selected all the *Fermi*-LAT data in daily (24 h) time intervals centred on each MAGIC observation. Similarly to the procedure used for the MAGIC observations (see Section 2.1), where no analysis were carried on individual observations/nights but were all stacked together, we stacked all the data from the daily-intervals around each MAGIC observation. The one-day interval was chosen so that there would be enough LAT exposure for source detection and spectral reconstruction. For this study, we adopted the same data selections and analysis procedure applied to the 12-yr analysis (see above for the analysis description).

2.3 KVA

In the optical band, the sources were monitored by a 35 cm Celestron telescope attached to the KVA telescope as a part of the Tuorla Blazar Monitoring Program (Takalo et al. 2008). The monitoring program started in 2002 and was originally focused on TeV candidate BL Lac objects from Costamante & Ghisellini (2002), but the monitoring sample has been gradually increasing throughout the years. The monitoring observations are typically performed twice a week. However, as most of the sources in this paper are not part of the main sample, the cadence of the observations is poorer in some cases. The observations were performed using the Cousins R-filter.

The data were analysed using the semi-automatic pipeline for differential photometry, developed for this purpose (Nilsson et al. 2018). For AO 0235+16, we used the comparison and control star magnitudes from Raiteri et al. (2007) while for other sources we calibrated the comparison stars using the observations of sources with known comparison star magnitudes from the same night.

---

[2] A Python package that facilitates analysis of LAT data with the *Fermi* Science Tools http://fermipy.readthedocs.io/en/latest/

[3] A measure of the quality of the direction reconstruction is used to assign events to four quartiles. The gamma-rays in Pass 8 data can be separated into four PSF event types: 0, 1, 2, 3, where PSF0 has the largest point spread function, and PSF3 has the best.

[4] https://fermi.gsfc.nasa.gov/ssc/data/access/lat/BackgroundModels.html
diffuse model: gll_iem_v07.fits and isotropic: iso_P8R3_SOURCE_V3_v1.txt

[5] The test statistic is the logarithmic ratio of the likelihood of a source being at a given position in a grid to the likelihood of the model without the source, TS = 2log(likelihood$_{src}$/likelihood$_{null}$) (Mattox et al. 1996).

As the sources have high redshift and bright optical nuclei, the contribution of the host galaxy to optical flux is negligible, and we did not correct for it. The measured magnitudes were corrected for galactic extinction using the galactic extinction model of Schlafly & Finkbeiner (2011).

2.4 *Swift*-UVOT and *Swift*-XRT

The *Neil Gehrels Swift Observatory* (Gehrels et al. 2004) is a space satellite launched in 2004 by the National Aeronautics and Space Administration (NASA). It is equipped with three telescopes, namely the UVOT (Roming et al. 2005), the Burst Alert Telescope (Barthelmy et al. 2005), and the XRT (Burrows et al. 2005), initially built to monitor the gamma-ray bursts and their afterglow phase, and then eventually developed into a versatile tool for collecting data in optical, UV, and X-rays from any source. Due to the presence of multiple instruments and rapid response to alerts, the *Swift* observatory is ideal for gathering simultaneous data in multiwavelength (MWL) campaigns.

In this work, we performed the spectral analysis contemporaneous to the MAGIC observations and derived the long-term LCs for two of the sources, namely CTA 102 and B2 2234+28A. Both sources were monitored in the U (345 nm), B (439 nm), and V (544 nm) optical bands and in the $UVW2$ (188 nm), $UVM2$ (217 nm), and $UVW1$ (251 nm) UV regime, as well as in X-ray energies between 0.3 and 10 keV. The comprehensive analysis was performed with heasoft.[6]

The *Swift*-UVOT instrumental magnitudes were calculated within a circular region centred at the source coordinates with a radius of 5 arcsec, using the UVOTSOURCE task. For the background determination, an annulus region centred at the same coordinates with an inner radius of 26 arcsec and an outer radius of 40 arcsec was used. The choice was made to prevent signal contamination from other sources in the closest vicinity of the studied blazars. Finally, we derived the fluxes taking into account the Galactic extinction A_V correction based on the hydrogen absorption column density N_H in the direction of the object and using the colour excess $E(B - V)$, calculated as $E(B - V) = N_H/(1.79 \times 10^{21} A_V)$ (Predehl & Schmitt 1995). The X-ray data reduction and calibration were performed using the standard procedure XRTPIPELINE.[7] Spectral fitting was carried out using XSPEC v.12.8.2 (Arnaud 1996) with a power-law model + Galactic absorption and in the energy range of 0.2–10 keV.

CTA 102 ($338°15$, $11°73$) was visible in three observation IDs, i.e. 00033509098, 00033509106, and 00033509110 for both UVOT and XRT. The LCs are generated with a longer time span from MJD 57624.9 to 57753.1 (2016-08-24 to 2016-12-31) based on 58 observation IDs between 00033509018 and 00088026001. The Galactic extinction was corrected with $N_H = 6.64 \times 10^{20}$ cm^{-2} (Evans 2014).

Just one observation with 00038408004 ID is available for B2 2234+28A ($339°09$, $28°48$) in the MAGIC time windows. While only one observation was considered for creating the broadband source spectrum, for the variability investigation, the LC was calculated between MJD 58641.1 and MJD 58668.3 (2019 June 07 to 2019 July 04) from two observations, namely 00038408002 and 00038408004. The Galactic extinction was corrected with $N_H = 6.15 \times 10^{20}$ cm^{-2} (Evans 2014).

3 SOURCE SAMPLE

While several observations of FSRQs with the MAGIC telescopes (MAGIC Collaboration 2008, 2021) resulted in the detection of gamma-ray emission, in this paper, we focus on the observations that have not resulted in a significant detection.

Most of the sources in this study have been observed by MAGIC as a target of opportunity (ToO): OP 313, AO 0235+16, 3C 454.3, TXS 0025+197, B2 22234+28A, B2 0234+28 following alerts of high activity of the sources in other wavelengths by the MWL partners, mainly *Fermi*-LAT. Moreover, 4C+55.17 and TXS 2241+406 were observed within the deep-exposure monitoring programme based on their average GeV emission in the preceding years.

The sources included in our study are listed in Tables 1 and 2. From Fig. 1, showing the gamma-ray flux versus spectral index for the extragalactic sources with known redshift contained in the 4LAC-DR3 (Ajello et al. 2022), it is possible to see that the sources selected in this work are among the brightest AGNs in the GeV domain.

Table 1 contains information about the studied sources based on the information in the 4FGL-DR2 catalogue, namely their coordinates and association, while variability index and the 12 yr integrated flux were estimated in this work. Finally the LAT flux values calculated during the data interval when the MAGIC telescopes observed the sources are reported. Table 2 provides information about the sources related to the analysis of data from the MAGIC telescopes, such as observation time (exposure), zenith angle range over which the source was observed, date of observations in MJD, the excess signal calculated using the Li & Ma (1983) prescription and the integral ULs.

In agreement with the preferred spectral model reported in the 4FGL-DR2 catalogue, most of the sources (except for 3C 454.3) studied in this paper are well described with an LP spectral model $\frac{dN}{dE} \propto E^{-\alpha + \beta \ln(E)}$ in the GeV range. For 3C 454.3, the spectrum is fitted with the power law with a superexponential cut-off model (PLSuperExpCutOff): $\frac{dN}{dE} \propto E^{-\gamma_1} \exp(-(E)^b)$.[8] The fit parameters are reported in Table 3.

All sources are classified as FSRQs in the *Fermi*-LAT 10-yr Source Catalog (4FGL-DR2), as well as in the latest 4FGL-DR4 (which is based on 14 yr of LAT data), except for AO 0235+16 (4FGL J0238.6+1637) which is classified as BL Lac in both data releases (see details below).

These sources were continuously observed by *Fermi*-LAT (see 12 yr LCs at Fig. A1) and KVA from 2008 to 2020. We compared the different flux states of each source by dividing the *Fermi*-LAT flux estimated during the MAGIC observations by the average flux over the whole 12 yr $\overline{\phi}_{HE,12}$ (see Table 1 as well as the following part on the individual source paragraphs).

3.1 Notes on individual sources

CTA 102 ($z = 1.037$, Schmidt 1965) is one of the most studied FSRQs in the MWL context, but still poorly investigated in the VHE band. High activity in gamma-rays was detected for the first time by the energetic gamma-ray experiment telescope (EGRET) onboard the Compton Gamma-Ray Observatory (Nolan et al. 1993). CTA 102 is one of the brightest FSRQs observed by *Fermi*-LAT. Strong gamma-ray outbursts have been observed from CTA 102 several times (see Raiteri et al. 2017; D'Ammando et al. 2019). From late 2016 to early 2017, CTA 102 exhibited an exceptional outburst that lasted for 4

---

[6] version 6.30
[7] https://heasarc.gsfc.nasa.gov/ftools/caldb/help/xrtpipeline.html

[8] For more information on the spectral model definitions see https://fermi.gsfc.nasa.gov/ssc/data/analysis/scitools/source_models.html

Table 1. *Fermi*-LAT FSRQs properties. Association, 4FGL name and coordinates (in J2000 reference frame) are taken from the 4FGL-DR2 catalogue, while flux and variability index were obtained by the *Fermi*-LAT analysis performed in this work. For the selected periods for the flux estimates during MAGIC observation, see Table 2.

Association name	4FGL source name	R.A. (°)	Decl. (°)	Integral flux (0.1–1000 GeV) $(10^{-8}\,\mathrm{cm}^{-2}\,\mathrm{s}^{-1})$	Variability index	Integral flux during MAGIC obs. (0.1–1000 GeV) $(10^{-8}\,\mathrm{cm}^{-2}\,\mathrm{s}^{-1})$
TXS 0025+197	J0028.4+2001	7.12	20.03	1.2 ± 0.2	28	63.4 ± 7.8
B2 0234+28	J0237.8+2848	39.46	28.80	16.7 ± 0.4	3220	80.3 ± 4.2
AO 0235+16	J0238.6+1637	39.67	16.62	13.1 ± 0.5	65	20.1 ± 5.1
4C+55.17	J0957.6+5523	149.42	55.38	8.5 ± 0.3	33	7.3 ± 1.0
OP 313	J1310.5+3221	197.65	32.35	3.7 ± 0.6	170	9.0 ± 5.1
CTA 102	J2232.6+1143	338.10	11.73	41.6 ± 0.6	14315	1030.0 ± 20.0
B2 2234+28A	J2236.3+2828	339.08	28.45	6.6 ± 0.3	388	16.9 ± 4.8
TXS 2241+406	J2244.2+4057	341.06	40.95	6.3 ± 0.4	3930	1.9 ± 1.7
3C 454.3	J2253.9+1609	343.49	16.15	215.0 ± 1.0	50905	261.0 ± 8.0

months, with the fluxes in all bands steadily increasing during the early stage of the high state. As a result, CTA 102 became one of the brightest gamma-ray sources in the sky at that moment (Balonek et al. 2016; Chapman et al. 2016; Ciprini 2016; Minervini et al. 2016). The MAGIC telescopes followed up CTA 102 during the very high state at the end of 2016 (the flux from *Fermi*-LAT was 20–30 times stronger than $\overline{\phi}_{\mathrm{HE,12}}$, the average flux for the source) and also during increasing activity in the HE range at the end of 2017 (the flux from *Fermi*-LAT was 10 times stronger than $\overline{\phi}_{\mathrm{HE,12}}$) for a total of ~3.5 h. The CTA 102 optical, UV, and X-ray LCs, demonstrating the source's heightened activity during the period of observation by the MAGIC telescopes, are displayed in Fig. 2. It also includes the LCs from MAGIC and *Fermi*-LAT.

3C 454.3 ($z = 0.859$; Paturel et al. 2002) is another well studied, highly variable FSRQ. The source was first detected in the GeV range by EGRET (Hartman et al. 1993). 3C 454.3 reached a high flux phase in 2000 and was extremely active in 2005 when it peaked at one of the highest optical brightness recorded from an AGN (Villata et al. 2006; Abdo et al. 2009a). *Fermi*-LAT reported strong and variable gamma-ray emission from this FSRQ in 2008 (Abdo et al. 2009a). In 2010, during the unusual bright gamma-ray flare, *Fermi*-LAT measured flux at $E > 100$ MeV to be $(66 \pm 2) \times 10^{-6}$ photons cm^{-2} s^{-1}. This was a factor of three higher than its previous maximum flux recorded in 2009 December (Abdo et al. 2011). At that time, 3C 454.3 was one of the brightest gamma-ray sources in the sky. The MAGIC-I telescope observed the source for the first time during the high states of 2007 July/August and November/December. The observation was carried out in mono mode. No significant emission was found, and the ULs were derived. The obtained data were consistent with the model based on the IC scattering of the ambient photons from the BLR by relativistic electrons, which predicted a sharp cut-off above 20–30 GeV due to the absorption of gamma-rays internally and the reduced effectiveness of the IC emission (Anderhub et al. 2009). Observations were carried out at different times when the state of the source varied considerably. In 2010 November, observations were taken when the source was most active, and the flux was 20 times greater than $\overline{\phi}_{\mathrm{HE,12}}$. In 2013 September, October, and November, the source had an average flux at or below $\overline{\phi}_{\mathrm{HE,12}}$. By 2014 June and July, the flux had risen to 2 to 4 times higher than $\overline{\phi}_{\mathrm{HE,12}}$. Furthermore, by 2015 August, the flux had further increased, roughly 3.5 times greater than $\overline{\phi}_{\mathrm{HE,12}}$. However, MAGIC observations resulted in no significant detection.

These observations, triggered by alerts from multiwavelength partners such as KVA and *Fermi*-LAT, emphasizing the time of the MAGIC observations, are depicted in Fig. A2. Following data selection, the total effective time of these observations amounted to 32 h.

OP 313 ($z = 0.997$; Schneider et al. 2010): In 2014, this blazar exhibited an upsurge in its activity in the GeV energy range, which led to its inclusion in the LAT Monitored Sources catalogue (Buson 2014). From 2019 onwards, an increase in the source's activity was observed once again, evident in both the optical (Balonek et al. 2019) and the gamma-ray bands (Hazra, Pal & Saha 2021). MWL LCs, focusing on the time of the MAGIC observations, are shown in Fig. A3. During these periods of high activity, the MAGIC telescopes gathered 12.3 h of good quality data (selection based on atmospheric transmission). Specifically, in 2014, the flux was documented as 11 times higher than the reference flux, $\overline{\phi}_{\mathrm{HE,12}}$. In 2019, the flux increased to 5 and 10 times that of $\overline{\phi}_{\mathrm{HE,12}}$. Despite these high activity periods, the MAGIC telescopes made no detections at that time.

In 2023 December, LST-1 detected high-energy gamma-ray emissions from OP 313 exhibiting a significant flux level of over 5

Table 2. Information on data collection by the MAGIC telescopes. For the exact time see Table A1.

Association name	Exposure (h)	Zenith (°)	MJDs – 50000	Significance of excess (σ)	ULs $E > 100\,\mathrm{GeV}$ ($10^{-12}\,\mathrm{cm}^{-2}\,\mathrm{s}^{-1}$)
TXS 0025+197	5.0	9–35	8728–8730; 8816–8818	0.2	13.0
B2 0234+28	25.6	0–36	8379–8481	1.6	4.4
AO 0235+16	6.1	11–26	7385–7400	0.7	20.9
4C+55.17	50.0	26–42	5512–5576, 6671–6777, 6993–7151, 57364	1.5	6.5
OP 313	13.6	4–39	6774–6811, 8654–8657, 8844–8849	− 0.5	9.2
CTA 102	3.2	17–42	7715–7740; 8105	1.7	62.4
B2 2234+28A	6.7	1–47	8352, 8639–8677	0.5	17.2
TXS 2241+406	29.5	22–35	7994, 8665, 8702–8756, 8805–8845	0.2	2.0
3C 454.3	34.6	12–48	5505–5509, 6561–6602, 6814–6864, 7257–57260	0.6	4.0
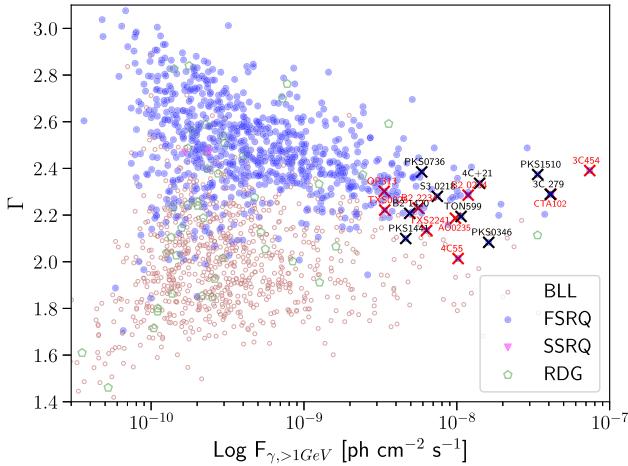
Figure 1. Diagram of the gamma-ray flux versus spectral index for the extragalactic sources with known redshift contained in the 4LAC-DR3 (Ajello et al. 2022). FSRQs already detected at VHE gamma-ray and reported in TeVCat (Wakely & Horan 2008), as well as the ones investigated in this project are indicated with crosses.

σ, corresponding to 15 per cent of the Crab Nebula's flux above 100 GeV (Cortina & CTAO LST Collaboration 2023). MAGIC also observed this source during that time. However, we do not use that data in this paper.

TXS 0025+197 ($z = 1.552$; Pâris et al. 2018) is the FSRQ with the highest redshift among the analysed sources. The *Fermi*-LAT observed an increased gamma-ray flux on 2019 August 14. Preliminary analysis indicates that the source reached a peak daily flux ($E > 100$ MeV) of $(1.0 \pm 0.2) \times 10^{-6}$ photons cm^{-2} s^{-1} (Buson 2019). MAGIC observed TXS 0025+197 in 2019 September and November–December, during an increased activity observed by *Fermi*-LAT in the gamma-ray band (with a flux 50–60 times higher than $\overline{\phi}_{\mathrm{HE},12}$) and collected 5 h of good quality data. The *Fermi*-LAT LC, focusing on the time of the MAGIC observation, is shown in Fig A4. Unfortunately, simultaneous optical KVA data were not available.

B2 2234+28A ($z = 0.790$, Shaw et al. 2012) displayed notable activity that the Guillermo Haro Observatory recorded. In particular, a significant increase in the source's luminosity in the near-infrared (NIR) band was detected. On 2010 November 26, the luminosity of the source in the NIR band increased approximately by a factor of 11 on a daily time-scale (Carrasco et al. 2010). Later in 2016, the same observation revealed a sixfold increase (Carrasco et al. 2016). MAGIC observed B2 2234+28A during its increased activity in the

optical and GeV energy bands observed by KVA and *Fermi*-LAT (flux ~ 1.3–2 times higher than $\overline{\phi}_{\mathrm{HE},12}$), respectively, in 2018 September and 2019 June/July and collected 6.7 h of good quality data. Fig. 3 illustrates the UVOT and XRT light curves, demonstrating that the source was undergoing a phase of amplified activity during the period of MAGIC observations.

B2 0234+28 ($z = 1.206$; Shaw et al. 2012): In 2018 October, the Special Astrophysical Observatory of the Russian Academy of Sciences reported a new active phase of the source, which increased its flux in the *R* band by a factor of 3 magnitudes with respect to its quiet state (Vlasyuk et al. 2018). The Guillermo Haro Observatory observed a flare in NIR on 2019 January 5. They reported that the source had increased its flux by 50 per cent (Carrasco et al. 2019). The increase in the flux level happened on a daily time-scale. MAGIC observed the source in 2018 and 2019 during its increased activity in the optical band. The source reached the highest flux in 2018 October which was 6–10 times higher than the average flux $\overline{\phi}_{\mathrm{HE},12}$ observed by *Fermi*-LAT. KVA and *Fermi*-LAT LCs are shown in Fig. A5, covering the time of MAGIC observation. MAGIC followed this source at that time and collected 25.6 h of data.

AO 0235+16 ($z = 0.94$; O'Meara et al. 2017): The classification of AO 0235+16 is not certain (Raiteri et al. 2007). It was one of the first objects classified as a BL Lac object (Spinrad & Smith 1975) and is still often classified as such. However, it has some characteristics of FSRQs, namely, strong emission lines have been detected in the spectra of A0 0235+16 during faint optical states (Cohen et al. 1987; Nilsson et al. 1996). The source is also strongly Compton-dominated during the flares, indicating that external seed photons must exist for the Compton scattering (Ackermann et al. 2012). At the end of 2014 and the beginning of 2015, the source showed unusually powerful optical and radio flares (Spiridonova et al. 2015; Vlasyuk et al. 2015). AO 0235+16 showed increased activity in the optical band at the end of 2015 and the beginning of 2016, triggering the MAGIC observations (see LC in Fig. A6). MAGIC collected a total of 6.1 h of good quality data.

4C+55.17 ($z = 0.902$; Pâris et al. 2018) is a bright *Fermi*-LAT FSRQ, which made the source a promising VHE emission candidate, due to high brightness and lack of strong variability (a low variability index is reported in all data releases of the 4FGL catalogues). MAGIC monitored this source in the VHE band (during the low state, flux below average $\overline{\phi}_{\mathrm{HE},12}$) from 2010 November to 2011 January for 28 h of good quality data. No significant VHE gamma-ray signal above 100 GeV was detected. Integral and differential ULs on the gamma-ray flux were derived (Aleksić et al. 2014). The VERITAS telescope also observed the source for 45 h between 2010 May and 2012 March. These observations also showed no significant VHE

Table 3. *Fermi*-LAT FSRQ fit model in the 4FGL catalogue and the results of the fit with a log parabola (LP) function (except of 3C 454.3, see text for details) to the *Fermi*-LAT data simultaneous to the MAGIC observations. The index b in the LAT analysis of 3C454.3 during MAGIC observations has been fixed for fit convergence.

Association name	Model	*Fermi*-LAT fit 4FGL		*Fermi*-LAT fit during MAGIC obs	
		α	β	α	β
TXS 0025+197	LP	2.092 ± 0.026	0.108 ± 0.015	2.53 ± 0.24	0.41 ± 0.19
B2 0234+28	LP	2.27 ± 0.02	0.0898 ± 0.0091	2.07 ± 0.06	0.10 ± 0.04
AO 0235+16	LP	2.080 ± 0.018	0.0954 ± 0.0095	1.67 ± 0.17	0.21 ± 0.09
4C+55.17	LP	1.901 ± 0.013	0.0767 ± 0.0067	1.93 ± 0.09	0.03 ± 0.04
OP 313	LP	2.282 ± 0.044	0.104 ± 0.0024	1.98 ± 0.23	0.26 ± 0.01
CTA 102	LP	2.261 ± 0.009	0.1007 ± 0.0060	1.95 ± 0.03	0.05 ± 0.01
B2 2234+28A	LP	2.273 ± 0.018	0.0898 ± 0.0091	1.72 ± 0.23	0.06 ± 0.07
TXS 2241+406	LP	2.088 ± 0.025	0.090 ± 0.013	2.13 ± 0.60	0.65 ± 0.56
3C 454.3	SuperExpPL	$-\gamma_1 = 2.014 \pm 0.010$	$b = 0.5183 \pm 0.0066$	$-\gamma_1 = -0.69 \pm 0.05$	$b = 0.5183$
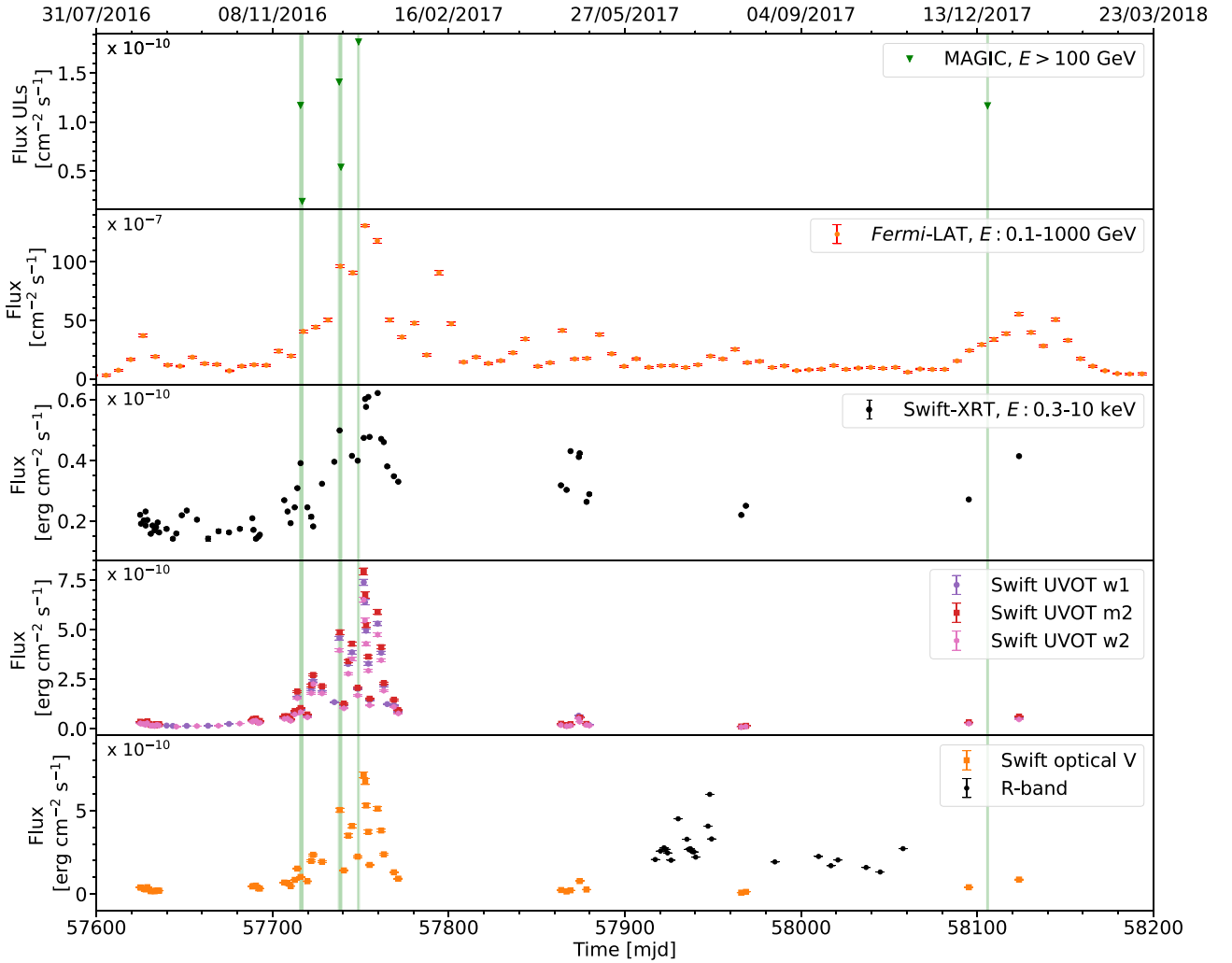
Figure 2. Light curve of CTA 102. The vertical areas indicate the days during which MAGIC observations were carried out. For *Fermi*-LAT LC, only points that met two criteria: a minimum test statistic (TS) value of nine and a signal-to-noise ratio greater than two were selected.

gamma-ray signal (Furniss & McConville 2013). Between 2008 and 2020, the source state was stable, as can be seen in A7. In this paper, old and new observations were merged to investigate this source in more detail at the VHE range. To carry out the analysis for this work, data from Aleksić et al. (2014) were combined with the MAGIC observations after 2011. After all 80 h of good quality data were obtained, including also 50 h of new data not previously published

when the source showed increased activity in the GeV energy range.

TXS 2241+406 ($z = 1.171$; Shaw et al. 2012): While being a promising candidate to emit VHE gamma rays, it also showed exceptional variability at past times. For the first time in 2015 February, *Fermi*-LAT observed a gamma-ray outburst from this source on a daily time-scale (Ojha & Carpen 2015).
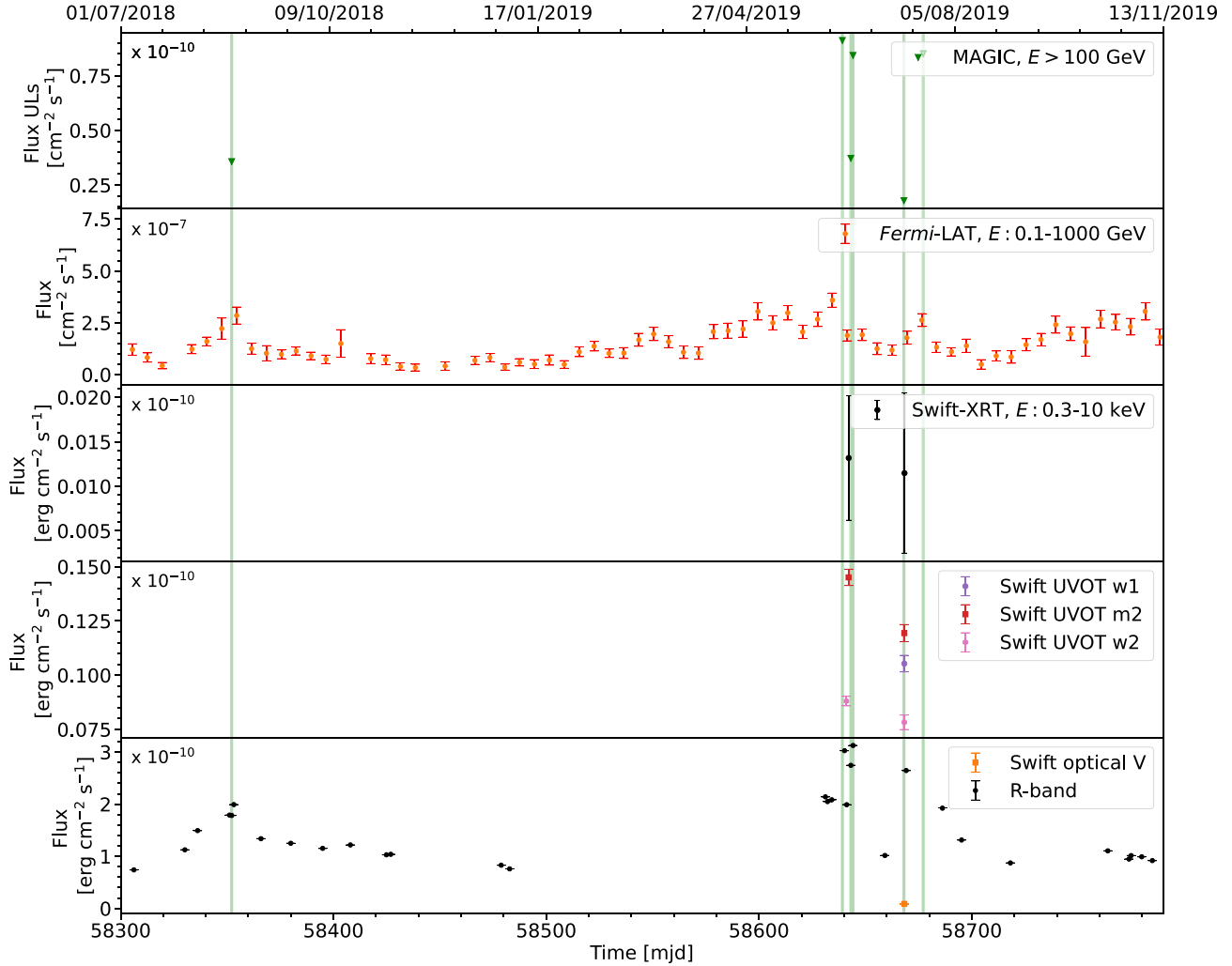
Figure 3. Light curve of B2 2234+28A. The vertical areas indicate the days during which MAGIC observations were carried out. For the *Fermi*-LAT LC, only points that met two criteria: a minimum TS value of nine and a signal-to-noise ratio greater than two are shown.

During that period, TXS 2241+406 was also monitored with KVA, showing optical variability spanning over 2.5 mag. As can be seen in the MWL LC (Figs A8 and A1), the variability of the source has significantly increased since 2015 compared to the previous six years of *Fermi*-LAT observations, encouraging monitoring with the MAGIC telescopes. In 2017 August, MAGIC followed this source for the first time and subsequently conducted a 27-h observational campaign from 2019 July to December. Unfortunately, during this period, the activity of the source was low, and it was either not detected by *Fermi*-LAT or the flux was below the average *Fermi*-LAT flux $\overline{\phi}_{HE,12}$.

4 RESULTS AND DISCUSSION

We investigated the MWL behaviour of these nine FSRQs contemporaneously with the MAGIC observations. We modelled the SED by utilizing data from *Fermi*-LAT telescope observations while accounting for redshift-dependent absorption by the EBL. Subsequently, we calculated the differential upper limits using data from the MAGIC telescopes, providing insights into the emission

properties and the possible additional absorption in the radiation field surrounding the jet, such as the BLR.

4.1 Gamma-ray emission

In Table 2, we report the MAGIC observation results for each of the nine FSRQs. We did not find any statistically significant signal ($> 5\sigma$ excess) for any sources in the VHE energy band. The statistically significant excess of gamma-rays was determined using the Li & Ma formula, as described in Li & Ma (1983). We performed simultaneous *Fermi*-LAT SEDs analysis according to the MAGIC observations. We calculated ULs with 95 per cent C.L. in five energy bins in the energy range from 50 to 500 GeV using MAGIC data, with assumed intrinsic spectral index of the gamma-ray photon distribution, $\alpha = 2.2$ for all sources.

The flux for each FSRQ is extrapolated to the VHE range from the *Fermi*-LAT data, considering the absorption of gamma-rays in the EBL as per the Domínguez et al. (2011) model Additionally, more recent EBL models (Franceschini & Rodighiero 2017; Saldana-Lopez et al. 2021) were also tested showing compatible results. This extrapolation operates under the assumption that there are no breaks in the photon spectra between HE and VHE due to
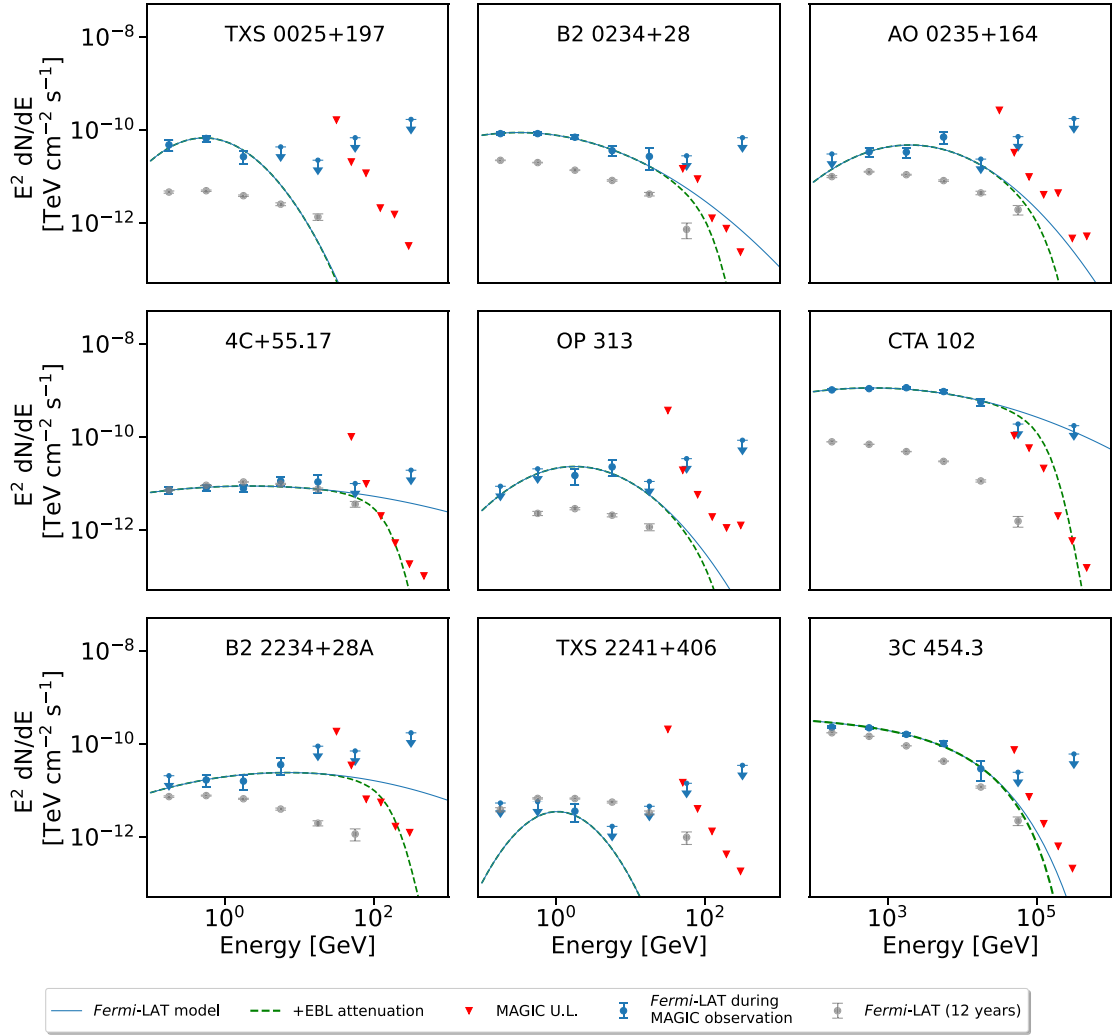
Figure 4. SED of all studied sources. The spectra of all studied sources that are simultaneous to MAGIC observations are fitted with log parabolic models (blue solid line) and extrapolated at VHE considering the EBL absorption (solid line). SED points (dots) from data collected by *Fermi*-LAT over a period of 12 yr to show the average state of each source are also included in the plots.

particle distribution cooling. Following this, the extrapolated model is compared to the MAGIC ULs. If the MAGIC upper limits are more constraining than such an extrapolation, it could suggest an absorption-induced cut-off in the VHE range. However, we note that it is possible that different flux states have been combined when the MAGIC and Fermi-LAT data were stacked, which could result in a mismatch in the source spectra between the HE and VHE data. The stacking of the data could, however, average out the HE and VHE gamma-ray data collected during what might have been different flux states.

The combined results of the *Fermi*-LAT analysis and the ULs from the MAGIC data analysis, along with the HE/VHE SED of all the investigated sources incorporating an EBL attenuation emission model, are presented in Fig. 4.

The calculated differential ULs for seven sources are consistent with the LP model extended from *Fermi*-LAT energy attenuated by EBL. Among them, for four sources, the MAGIC ULs lie above the *Fermi*-LAT extrapolated model, and for three of the sources, the ULs are close to the *Fermi*-LAT extrapolated model. Regarding the other two sources, B2 2234+28A and CTA 102, the MAGIC

ULs around 100 GeV are below the *Fermi*-LAT EBL extrapolation model. Therefore, those two objects are plausible candidates for sources in which absorption in BLR could introduce an extra cut-off from absorption in the BLR. We further investigate this possibility in the next Section 4.2 and focus on these two sources.

4.2 Modelling

As a result of our analyses, two sources, B2 2234+28A and especially CTA 102, showed a hint of cut-off in the HE/VHE SED that cannot be explained only by the EBL absorption. In the case of B2 2234+28A, if we also consider uncertainties with the EBL extrapolation, the EBL absorption might explain the cut-off; in the case of CTA 102, the cut-off is more robust. Subsequently, we investigated the possibility of additional absorption in the BLR for these two sources.

The simple empirical stratified BLR model from Finke (2016) is applied. It relies on the reverberation mapping method of AGNs (Bentz et al. 2009; Bentz 2016). It assumes that accretion disc radiation is absorbed by the BLR clouds surrounding the emission and is re-emitted as monochromatic lines at an established distance

from the BH. A similar approach was used in a study of 3C 279 (H. E. S. S. Collaboration 2019).

Our BLR model comprises 26 concentric infinitesimally thin spherical shells containing gas emitting a range of emission lines, from Ly ϵ to H α. The radius and the luminosity of individual lines of the BLR are required to calculate the gamma-ray absorption and for further broad-band SED modelling.

We estimated the disc luminosity, $L_{\rm disc}$, from the luminosity of a single line, assuming that the entire BLR luminosity is 10 per cent of the disc luminosity. We used the measured H β emission line as a reference to estimate the radii of individual lines in the BLR. All other shell luminosities and radii were scaled according to the relative luminosity of the disc and the measured Mg line. To achieve this, we employed the following relation (based on reverberation mapping of AGN objects):

$$R(\mathrm{H}\beta) = 10^{16.94 \pm 0.03} \left(\frac{L(5100\text{Å})}{10^{44}\,\mathrm{erg\,s}^{-1}} \right)^{0.533 \pm 0.035} \mathrm{cm},$$

$$\left(\frac{L(5100\text{Å})}{10^{44}\,\mathrm{erg\,s}^{-1}} \right) = \left(\frac{L(\mathrm{H}\beta)}{(1.425 \pm 0.007) \times 10^{42}\,\mathrm{erg\,s}^{-1}} \right)^{0.8826 \pm 0.0039}$$

as described in Greene & Ho (2005) and Bentz et al. (2013).

In our estimation, we used the relative line luminosities $L(\mathrm{Mg\,II})$ from Paliya et al. (2021) and converted these values using the broad-emission line parameters from Finke (2016), assuming a ratio of $L(\mathrm{Mg\,II})/L(\mathrm{H}\beta) = 1.7$. Using this method, we derived the luminosity $L_{\mathrm{H}\beta}$ and radius $R_{\mathrm{H}\beta}$ for the H β line for CTA 102: $L_{\mathrm{H}\beta} = 6.7 \times 10^{43}\,\mathrm{erg\,s}^{-1}$ and $R_{\mathrm{H}\beta} = 5.13 \times 10^{17}\,\mathrm{cm}$. Similarly, for B2 2234+28A, we obtained $L_{\mathrm{H}\beta} = 1.62 \times 10^{43}\,\mathrm{erg\,s}^{-1}$ and $R_{\mathrm{H}\beta} = 2.67 \times 10^{17}\,\mathrm{cm}$. The distances and luminosities of the remaining lines are scaled. To determine the radii and luminosities of other lines, we use the values from table 5 in Finke (2016). The absorption in the BLR was calculated over all lines from table 5 in Finke (2016). We calculated the BLR absorption using the *agnpy*[9] modelling package (Nigro et al. 2022). Concerning analytical speed and improved numerical accuracy when dealing with the multidimensional integration, methods from *cubepy*[10] were implemented in *agnpy* for those calculations.

The methodology approach to constrain the distance between the black hole, (note that BLR is assumed to be concentric with the BH position) and the emission region (a blob) $R_{\rm blob,\,BLR}$, and to check its consistency using the broad-band model involves two types of models. First, modelling the SED in the HE and VHE ranges (*Fermi*-LAT flux measurements and MAGIC ULs) allows us to estimate $R_{\rm blob,\,BLR}$. This is done using a phenomenological model that constrains the location of the emission region. The absorption in the BLR radiation field is introduced, and the resulting spectrum is compared with the MAGIC ULs on the flux. Secondly, we consider a broad-band emission model, which tests the underlying blazar physics and parameters from the phenomenological study. This broad-band emission model is used to check the consistency of the previous results obtained using the phenomenological model. The approach we are following involves using the phenomenological model to estimate the distance between the black hole and the emission region, and then using the broad-band model to test the underlying physics and parameters to ensure consistency with the previous results.

4.2.1 Phenomenological model

The contemporaneous observations of CTA 102 and B2 2234+28A by *Fermi*-LAT and MAGIC telescopes allowed for a combination of the *Fermi*-LAT spectral fit and the MAGIC ULs to constrain the minimum distance of the emission regions to the black hole, $R_{\rm blob,\,BLR}$. For this purpose, the absorption features caused by pair production of gamma-rays with photons of the BLR in SED are used.

To constrain the distance of the emission region from the black hole, we used the *Fermi*-LAT fit model, considering both EBL and BLR absorption. We vary the BLR absorption level by varying the distance of the emission region from the black hole with steps of 0.1 $R_{\mathrm{H}\beta}$. By comparing this fit model with EBL and BLR absorption with the measured ULs, we can put constraints on the location of the emission region from the black hole.

Fig. 5 shows the gamma-ray SEDs from CTA 102 and B2 2234+28A, The two sources for which an additional steepening is caused by internal absorption need to be consistent with the VHE ULs.

The *absorption* module and the *Spherical Shell BLR* geometry from the *agnpy* package were used to construct the phenomenological model. Under the assumption that the steepening/cut-off of the gamma-ray emission in the VHE band is due to the absorption in the BLR, we place a constraint on the maximum distance between the black hole and the emission region $R_{\rm blob,\,BLR}$. For CTA 102, we obtain $R_{\rm blob,\,BLR} < 1.5 \times R_{\mathrm{H}\beta}$ (where $R_{\mathrm{H}\beta} = 7.7 \times 10^{17}$ cm) and for B2 2234+28A we got $R_{\rm blob,\,BLR} < 1.6 \times R_{\mathrm{H}\beta}$ (where $R_{\mathrm{H}\beta} = 4.3 \times 10^{17}$ cm). It is important to note that the presence of a cut-off in the gamma-ray spectrum at high energies does not always indicate absorption in the BLR. Other factors, such as the cut-off in the emitting particle distribution, can also explain this phenomenon (Costamante et al. 2018).

The dependence of the integrated disc radiation reprocessed in all the shells located farther than a given distance of the emission region is shown in Fig. 6. The plot indicates that explaining the non-detection of VHE gamma-ray emission as an effect of the absorption in the BLR requires at least a value as low as $R_{\rm blob,\,BLR}$ as the derived value. The distance is large enough that the emission region is within the outermost part of the BLR. However, even this location provides sufficient absorption to explain the *Fermi*-LAT and MAGIC data, assuming that the emission region is located beyond most of the shells that construct BLR.

4.2.2 Broad-band modelling

In the previous section, we determined the distance between the emission region and the black hole, denoted as $R_{\rm blob,\,BLR}$, in a phenomenological way based on observations made by the *Fermi*-LAT and MAGIC telescopes. We now compare these obtained values with a physical model that describes the broad-band emission of the jet.

In modelling the gamma-ray emission from FSRQs, one-zone SSC and EC models are commonly used. It is assumed that the central engine is surrounded by clouds rescattering emission from the accretion disc, with a dust torus (DT) around the BLR. The simplified one-zone leptonic model may not fully represent the complex conditions within the jet, and the detection of VHE gamma-rays from some FSRQs suggests that the emission region cannot be deeply located within the BLR (Zacharias 2018).

Given that our source does not exhibit significant VHE photon emission, the most straightforward target for the EC model would be the BLR radiation field, which strongly absorbs VHE gamma-rays
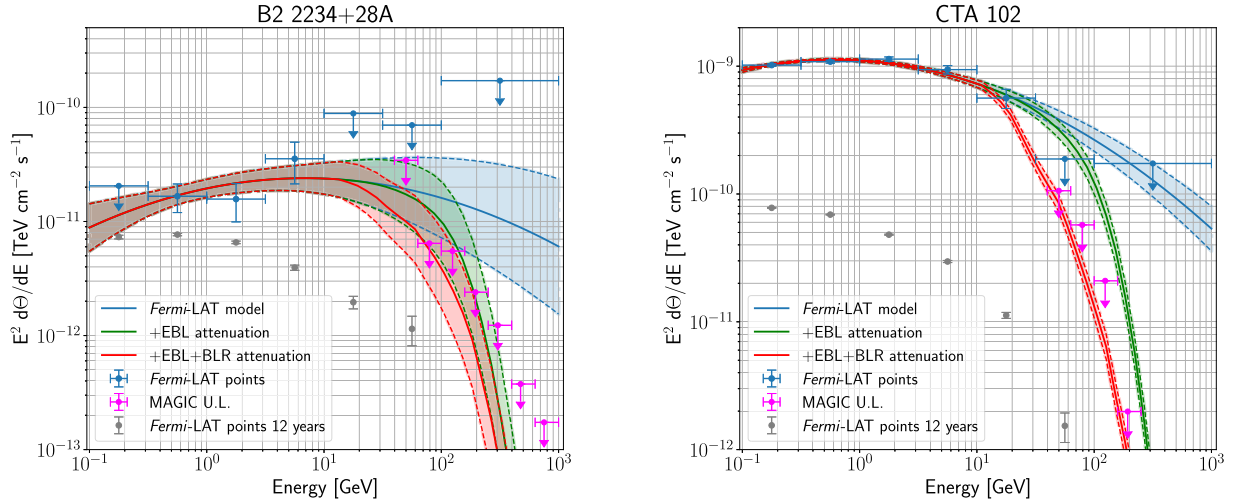
Figure 5. SED of B2 2234+28A (on the left) and CTA 102 (on the right) in the HE and VHE range: derived VHE differential upper limits (95 per cent C.L.) on the flux by MAGIC and *Fermi*-LAT spectrum obtained during the MAGIC observation period. A blue solid line depicts a spectral fit with the LP model. The intrinsic *Fermi*-LAT spectrum attenuated with Dominguez's EBL model (Domínguez et al. 2011) is shown with a green line. The red line shows the spectrum after considering absorption on multiple BLR lines. The spectra points of B2 2234+28A and CTA 102 obtained in 12 yr of *Fermi*-LAT observations are also shown (grey dots). The spectrum is shown taking into account the uncertainty of the parameters obtained when fitting the data (shaded region).
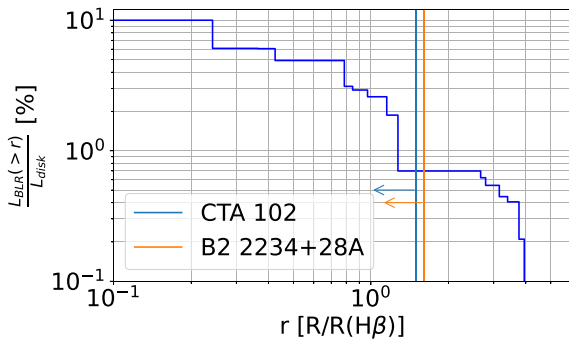
Figure 6. Fraction (in blue) [per cent], $L_{BLR}(r)/L_{disc}$, of the disc radiation reprocessed in shells located farther than the distance r from the black hole, according to the used BLR model. The distance from the emission region is normalized to the radius of the Hβ line. Vertical lines show the derived maximum distance from the black hole for the two studied sources to have sufficient BLR absorption to explain the lack of the observed VHE gamma-ray emission.

in the sub-TeV range. We assembled data from KVA, *Swift*-UVOT, *Swift*-XRT, *Fermi*-LAT, and ULs from the MAGIC telescopes to construct broad-band SEDs of B2 2234+28A and CTA 102. Both sources are modelled in a framework of a simple one-zone leptonic model with *agnpy*, in which a spherical emission region with a radius R_{blob} is isotropically and homogeneously filled with a magnetic field B and electrons. The electron spectrum spans from γ_{min} to γ_{max} with indices p_1 and p_2 below and above the break at γ_b and is described by a broken power-law electron energy distribution with spectral normalization K_e, differential number density at γ_b. The single emission region moves along the jet with the bulk Lorentz factor Γ at an angle θ to the line of sight, causing the corresponding Doppler factor δ_D. In our model, we assume that the emission region is situated at a distance that explains the steepening of emission due to the absorption as a result of the phenomenological study (see Section 4.2.1).

In our model, the external radiation field includes multiple lines from the BLR shells and thermal IR radiation from the DT. Additionally, synchrotron and SSC processes are responsible for

emission in the radio to GeV energy range Finke (2016). The DT is represented as an infinitesimally thin ring with temperature $T_{dt} = 10^3$ K, the radius of the torus R_{dt} is estimated from equation (96) in Finke (2016), and the efficiency of reprocessing disc radiation in DT is set on commonly used value $\xi_{dt} = 0.6$ (see e.g. Acciari et al. 2022). We ensure that the DT thermal luminosity is below the non-thermal synchrotron one. The single-temperature blackbody radiation computed with *agnpy* is used to assess if the DT emission is significantly lower in magnitude compared to the synchrotron emission.

Our model assumes that the emission region is outside most of the shells in the BLR, as shown in Fig. 6. The radius of the emission region is established according to the formula $R_{blob} = R_{blob, BLR}/\Gamma$, i.e. assuming a conical jet with a half-opening angle of $\sim 1/\Gamma$.

For CTA 102, we selected a Doppler factor δ of 40, based on very long baseline interferometry studies, which established it at 34 ± 4 to explain HE emissions (Casadio et al. 2019). For B2 2234+28A, we used $\delta = 13$ as a weighted average Doppler factor value for the FSRQ from *VLBA-BU-BLAZAR* study (Jorstad et al. 2017).

The model parameters (K_e, p_1, γ_b, γ_{max}, B) were estimated by fitting the SED with the open source package *gammapy* (Deil et al. 2017) using a *Synchtron*, *SynchrotronSelfComtpon*, and *External-Compton* modules from *agnpy*. We assume a classical cooling break setting $p_2 = p_1 + 1$. The fitting procedure was performed, taking into account a simplified systematic error on the flux points. We use a conservative estimation of the systematic errors, i.e. 10 per cent for the HE and X-ray instruments and 5 per cent for the optical telescopes. The result of the fitting is shown in Fig 7, while the parameters are given in Table 4. The absorption processes in both EBL and BLRs affect the modelling and interpretation of the data. The modelling results are corrected by considering the absorption on those two radiation fields (red solid line).

We evaluated the jet power corresponding to the parameters obtained from the agnpy model fit. For B2 2234+28A, the jet power in particles is 0.93×10^{45} erg s^{-1}, and the jet power in the magnetic field is 0.37×10^{45} erg s^{-1}. For CTA 102, the jet power in particles is 2.52×10^{45} erg s^{-1}, and the jet power in the magnetic field is 5.52×10^{45} erg s^{-1}. We compare these values with data from Kim et al. (2022), specifically for CTA 102 from 2017 March 28
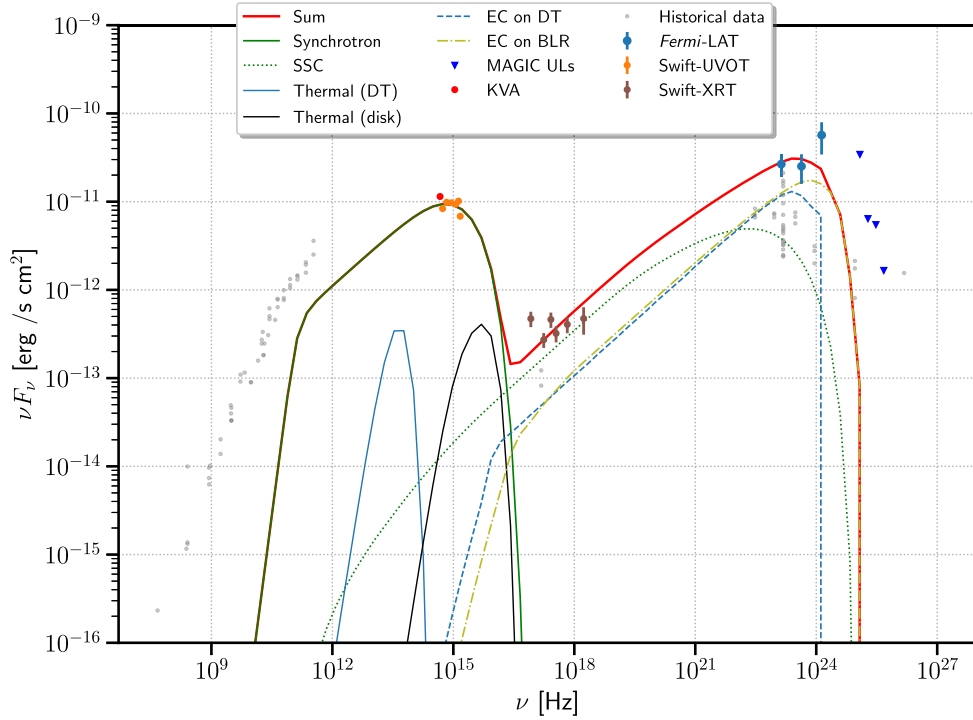
(a) B2 2234+28A
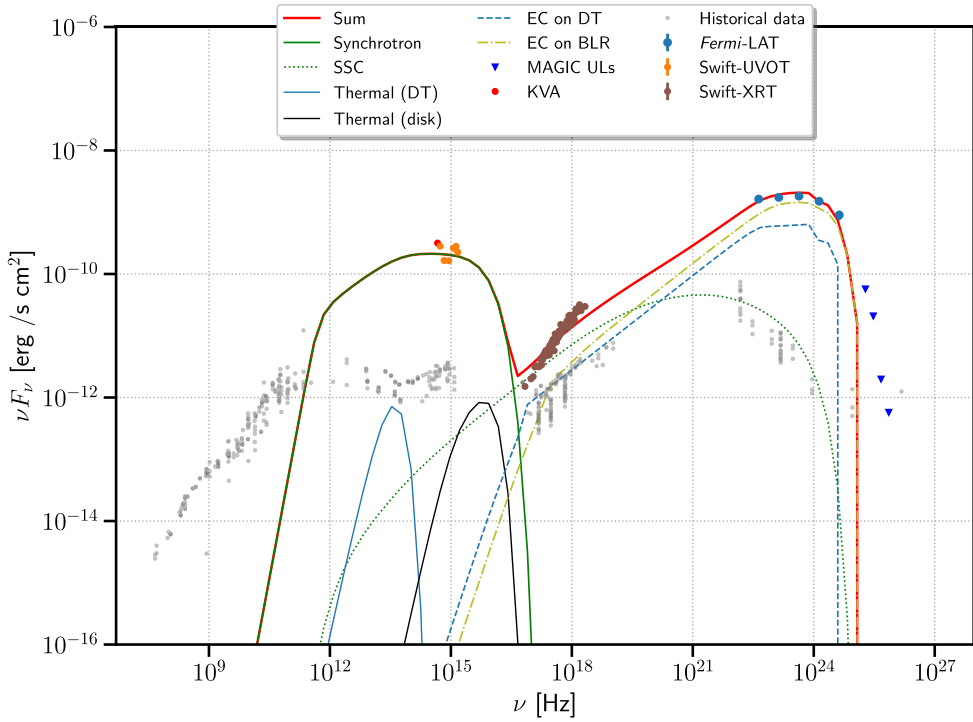
(b) CTA 102

Figure 7. Broad-band modelling with agnpy of B2 2234+28A (top panel) and CTA 102 (bottom panel). The solid red line shows the overall emission modelled. The low-energy peak is dominated by synchrotron radiation (solid line), and the high-energy peak is dominated by the emission produced in the external Compton mechanism using the seed photons from infrared dusty torus (dashed line) and broad-line region produced in 26 shells (dash–dotted line). Grey points–archival data from the Space Science Data Center – ASI.

Table 4. Parameters used for modelling sources with agnpy, utilizing an emission region represented as a blob, DT, and BLR. Parameters such as K_e, $p1$, γ_b, γ_{max}, and B were derived during the fitting process. R_{blob} was estimated using the phenomenological model. The remaining parameters were fixed according to the information gathered from the literature. Mass for both sources were taken from Paliya et al. (2021).

parameter	CTA 102	B2 2234+28A
Mass (10^8 M$_\odot$)	12.30	2.75
$R_{blob, BLR} < (R_{H\beta})$	1.5	1.6
L_{disc} (10^{45} erg s^{-1})	20.49	4.95
Emission regions		
$p1$	1.97 ± 0.02	2.18 ± 0.08
$p2$	2.97	3.18
δ_D	40	13
R_{blob} (10^{15} cm)	28.5	20.8
K_e (10^{-5} cm^{-3})	546 ± 24	4.47 ± 0.05
Γ	20.5	7
γ_b	850 ± 2	5929 ± 271
γ_{min}	1	1
γ_{max}	8616 ± 19	$16\,292 \pm 4021$
B (Gauss)	1.12 ± 0.04	0.52 ± 0.03
Dusty Torus		
ξ_{dt}	0.6	0.6
T_{dt} (K)	1000	1000
R_{dt} 10^{17} (cm)	159	78
Broad-line region		
$R_{H\beta}$ (10^{17} cm)	5.13	2.67
$L_{H\beta}$ (10^{43} erg s^{-1})	6.7	1.62
ξ	0.1	0.1
U_e (erg cm^{-3})	0.022	0.027
U_B (erg cm^{-3})	0.047	0.011

(the closest in time to the MAGIC data), where a jet power for the magnetic field $< 0.28 \times 10^{45}$ erg s^{-1} and for particles $> 1.08 \times 10^{47}$ erg s^{-1} is reported. This comparison reveals a significant discrepancy: our modelling results show an order of magnitude higher power in particles and an order of magnitude lower power in the magnetic field. Nevertheless, it is important to consider that the values from Kim et al. (2022) are derived from the synchrotron-self-absorbed radio core region, expected at approximately parsec scales, which is an order of magnitude farther than the region considered in our modelling. Additionally, we compare the jet kinetic power values with Nemmen et al. (2012). According to their study, CTA 102 has a jet kinetic power of 5.24×10^{45} erg s^{-1}, and B2 2234+28A has a jet kinetic power of 1.90×10^{45} erg s^{-1}. These values, derived using the relation with gamma-ray luminosity by Xiong & Zhang (2014), show good consistency (within a factor of a few) with those obtained from our modelling.

We had a constraint that the distance between the emission region and the black hole had to be $< 1.5 \times R_{H\beta}$ for CTA 102, and $< 1.6 \times R_{H\beta}$ for B2 2234+28A from the previous section. Broad-band modelling with the leptonic model performed in this section indicates that we may be able to reconstruct the observations with constraints from the phenomenological model.

5 SUMMARY AND CONCLUSIONS

This paper presents a catalogue of upper limits for nine FSRQs observed by the MAGIC telescopes over the last 10+ yr, resulting in a total observation time of 174 h for all the sources. All investigated sources are at large redshifts ($z \sim 1$).

We compared the limits on the VHE gamma-ray emission of these sources derived with the MAGIC telescopes with the extrapolation of the contemporaneous GeV emission seen by *Fermi*-LAT, taking into account the absorption by the EBL. For four out of nine investigated sources (namely TXS 0025+197, AO 0235+164, OP 313, and TXS 2241+406), the MAGIC telescopes ULs lie above the emission predicted by the model, which was constructed from the extrapolation of the *Fermi*-LAT observations. For the other three sources (4C+55.17, 3C 454.3, and B2 0234+28), the spectra, after accounting for absorption in the EBL, are close to the ULs obtained by MAGIC (see Fig. 4). The fact that for these seven sources, the MAGIC ULs lie very close to or above the *Fermi*-LAT extrapolated model does not allow us to set any additional constraints on the absorption by the BLR. Their large redshift distances could explain the lack of detection in the VHE range for these sources. It may also be due to the fact that there is a certain delay between the emission enhancement triggering the ToO and the time when pointing instruments, such as the MAGIC telescopes, start their observations, which can also be additionally limited by atmospheric conditions or moonlight.

Lastly, for two sources, B2 2234+28A and CTA 102, we obtained with the MAGIC telescopes ULs on the flux below the emission predicted by the *Fermi*-LAT extrapolation model, which could suggest the presence of an additional absorption from the BLR. As shown in Fig. 6, the required absorption in BLR to explain the constraints derived by the MAGIC telescopes for both sources requires a weak absorption of only 1 per cent of the disc luminosity corresponding to the distance between the emission region and the black hole in both cases at the edge of the BLR, namely $\lesssim 1.6 \times R_{H\beta}$. This agrees with findings for another FSRQ object in Wendel, Shukla & Mannheim (2021), which suggest that the gamma-ray emission located in 3C 279 most likely originates from the edge of the BLR.

We investigated two approaches: a phenomenological description of the gamma-ray band spectral shape and a fitting of a broad-band radiative model. The first was limited to the HE and VHE gamma-ray range and was used to derive a constraint on the distance between the emission region and the black hole. The second approach instead considers the emission over the whole spectrum, where the constraint from the phenomenological approach was tested in a leptonic emission model. Based on the SED shown in Fig. 7, it can be said that the major contribution to the HE emissions from the two sources, B2 2234+28A and CTA 102, studied in this work is the combination of the EC processes on the DT and the BLRs. The data fitting process yielded the values of parameters that describe the broad-band emission model. For CTA102 and B2 2234 + 28A, the magnetic field energy density (U_B) and the total electron energy density (U_e) are observed to be comparable. Jets are believed to be born dominated by the Poynting flux, i.e. the electromagnetic field. The magnetic fields are then crucial in the process of accelerating particles to non-thermal spectra (either in diffusive shock acceleration or magnetic reconnection); thus, along the jet, conversion of magnetic energy into kinetic energy occurs. The equipartition of the magnetic and kinetic energy is, therefore, often postulated in theoretical models as the most natural way of identifying the region of the source in which such energy conversion occurs most efficiently.[11]

It is important to note that the conclusion drawn is highly dependent on the model used. Based on our phenomenological

---

[11]Some models, however, report large deviation from equipartition, e.g. MAGIC Collaboration (2020).

model, our analysis of the observations made on CTA 102 and B2 2234+28A in the HE and VHE ranges leads us to conclude that the absorption in the BLR is weak. Furthermore, the model's best-fitting solution, which considers the full broad-band spectrum, is consistent with the ULs set by MAGIC. This consistency can be attributed to the limited energy range of the electrons. The broad-band modelling, when considering the assumed distance of the emission region, agrees with the observations from the MAGIC telescopes. Therefore, we can infer that the observed steepening at VHE energies is primarily due to the characteristics of the particle distribution, such as its maximum energy or distribution slope, rather than being significantly influenced by absorption effects. These observations are consistent with the study performed with the *Fermi*-LAT telescope, which found no evidence for the expected BLR absorption (Costamante et al. 2018). It is crucial to note that location constraints based on a naive extrapolation of the *Fermi*-LAT spectrum may not be robust. This is because we cannot assume the intrinsic spectrum to behave straightforwardly, which should be considered in future studies, such as those with CTA (Mazin 2019) data. The lack of evidence for strong absorption of the VHE gamma-ray radiation in FSRQs is promising for future observations with the present and next generation of IACTs.

ACKNOWLEDGEMENTS

DATA AVAILABILITY

Data will be made available on request.

REFERENCES

Anderhub H. et al., 2009, A&A, 498, 83
Abdo A. A. et al., 2009a, ApJ, 699, 817
Abdo A. A. et al., 2009b, Phys. Rev. D, 80, 122004
Abdo A. A. et al., 2011, ApJ, 733, L26
Abdollahi S. et al., 2020, ApJS, 247, 33
Abdollahi S. et al., 2022, ApJS, 260, 53
Acciari V. A. et al., 2022, MNRAS, 510, 2344
Ackermann M. et al., 2012, ApJ, 751, 159
Ackermann M. et al., 2016, ApJS, 222, 5
Aharonian F. et al., 2008, A&A, 478, 387
Ahnen M. L. et al., 2015, ApJ, 815, L23
Ahnen M. L. et al., 2016, A&A, 595, A98
Ajello M. et al., 2017, ApJS, 232, 18
Ajello M. et al., 2022, ApJS, 263, 24
Aleksić J. et al., 2011a, ApJ, 742, 43
Aleksić J. et al., 2011b, ApJ, 730, L8
Aleksić J. et al., 2012, Astropart. Phys., 35, 435
Aleksić J. et al., 2014, MNRAS, 440, 530
Aleksić J. et al., 2016a, Astropart. Phys., 72, 61
Aleksić J. et al., 2016b, Astropart. Phys., 72, 76
Angioni R., 2018, Astron. Telegram., 11251
Archambault S. et al., 2016, AJ, 151, 142
Arnaud K. A., 1996, Jacoby G. H., Barnes J., eds, ASP Conf. Ser. Vol. 101, Astronomical Data Analysis Software and Systems, Astron. Soc. Pac., San Francisco, p. 17

Atwood W. B. et al., 2009, ApJ, 697, 1071

Balonek T. J. et al., 2016, Astron. Telegram, 9732

Balonek T. J., Santos M. D. L., Dougherty D., Ishraque F., Liberman J., Slater J., 2019, Astron. Telegram, 12898

Barthelmy S. D. et al., 2005, Space Sci. Rev., 120, 143

Bentz M. C., 2016, Astronomy at High Angular Resolution, Vol. 439, Astrophysics and Space Science Library, Springer International Publishing, Switzerland, p. 249

Bentz M. C., Peterson B. M., Netzer H., Pogge R. W., Vestergaard M., 2009, ApJ, 697, 160

Bentz M. C. et al., 2013, ApJ, 767, 149

Böttcher M., 2007, in Ho L. C., Wang J.-M., eds, ASP Conf. Ser. Vol. 373, The Central Engine of Active Galactic Nuclei, Astron. Soc. Pac., San Francisco, p. 169

Buson S., 2014, Astron. Telegram, 6068

Buson S., 2019, Astron. Telegram, 13032

Bruel P., Burnett T. H., Digel S. W., Johannesson G., Omodei N., Wood M., 2018, preprint (arXiv:1810.11394)

Burrows D. N. et al., 2005, Space Sci. Rev., 120, 165

Carrasco L., Carramiñana A., Escobedo G., Recillas E., Valdes J. R., Porras A., Mayya Y. D., 2010, Astron. Telegram, 3056

Carrasco L., Recillas E., Porras A., Chavushyan V., Mayya D. Y., Carraminana A., 2016, Astron. Telegram, 8572

Carrasco L., Escobedo G., Porras A., Recillas E., Chavushyan V., 2019, Astron. Telegram, 12401

Casadio C. et al., 2019, A&A, 622, A158

Chapman K. J., Sabyr A., Stahlin R. W., Zhang S., Balonek T. J., 2016, Astron. Telegram, 9756

Cohen R. D., Smith H. E., Junkkarinen V. T., Burbidge E. M., 1987, ApJ, 318, 577

Cortina J., CTAO LST Collaboration, 2023, Astron. Telegram, 16381

Costamante L., Ghisellini G., 2002, A&A, 384, 56

Costamante L., Cutini S., Tosti G., Antolini E., Tramacere A., 2018, MNRAS, 477, 4749

Ciprini S., 2016, Astron. Telegram, 9869

Dazzi F. et al., 2021, IEEE Trans. Nucl. Sci., 68, 1473

D'Ammando F. et al., 2019, MNRAS, 490, 5300

Deil C. et al., 2017, Proc. Sci., 35th International Cosmic Ray Conference (ICRC2017), SISSA, Trieste, PoS#766

Dermer C. D., 2013, Astrophysics at Very High Energies, Vol. 40, Saas-Fee Advanced Course. Springer-Verlag, Berlin, p. 225

Dermer C. D., Schlickeiser R., 2002, ApJ, 575, 667

Evans P. A. et al., 2014, ApJ, 210, 8

Domínguez A. et al., 2011, MNRAS, 410, 2556

Falcone A. D. et al., 2004, ApJ, 613, 710

Finke J. D., 2016, ApJ, 830, 94

Finke J. D., Razzaque S., Dermer C. D., 2010, ApJ, 712, 238

Finke J. D., Ajello M., Domínguez A., Desai A., Hartmann D. H., Paliya V. S., Saldana-Lopez A., 2022, ApJ, 941, 33

Fomin V. P., Stepanian A. A., Lamb R. C., Lewis D. A., Punch M., Weekes T. C., 1994, Astropart. Phys., 2, 137

Furniss A., McConville W., 2013, preprint (arXiv:1303.1103)

Franceschini A., Rodighiero G., 2017, A&A, 603, A34

Gehrels N. et al., 2004, ApJ, 611, 1005

Gerasimova N. M., Nikishov A. I., Rosenthal I. L., 1962, J. Phys. Soc. Japan, 17, 175

Greene J. E., Ho L. C., 2005, ApJ, 630, 122

Hartman R. C. et al., 1993, ApJ, 407, L41

Hazra M., Pal S., Saha D., 2021, Astron. Telegram, 14404

H. E. S. S. Collaboration, 2014, A&A, 564, A9

H. E. S. S. Collaboration, 2019, A&A, 627, A159

Hovatta T., Lindfors E., 2019, New Astron. Rev., 87, 101541

Jorstad S. G. et al., 2017, ApJ, 846, 98

Kim S.-H. et al., 2022, MNRAS, 510, 815

Li T.-P., Ma Y.-Q., 1983, ApJ, 272, 317

Liu H. T., Bai J. M., 2006, ApJ, 653, 1089

MAGIC Collaboration, 2008, Science, 320, 5884.1752

MAGIC Collaboration, 2020, MNRAS, 492, 5354

MAGIC Collaboration, 2021, A&A, 647, A163

Mattox J. R. et al., 1996, ApJ, 461, 396

Mazin D., 2019, Proc. Sci., 36th International Cosmic Ray Conference (ICRC2019). SISSA, Trieste, PoS#741

Meyer M., Scargle J. D., Blandford R. D., 2019, ApJ, 877, 39

Minervini G. et al., 2016, Astron. Telegram, 9743

Nolan P. L. et al., 1993, ApJ, 414, 82

Nemmen R. S., Georganopoulos M., Guiriec S., Meyer E. T., Gehrels N., Sambruna R. M., 2012, Science, 338, 1445

Nigro C., Sitarek J., Gliwny P., Sanchez D., Tramacere A., Craig M., 2022, A&A, 660, A18

Nilsson K., Charles P. A., Pursimo T., Takalo L. O., Sillanpaeae A., Teerikorpi P., 1996, A&A, 314, 754

Nilsson K. et al., 2018, A&A, 620, A185

Ojha R., Carpen B., 2015, Astron. Telegram, 8319

O'Meara J. M., Lehner N., Howk J. C., Prochaska J. X., Fox A. J., Peeples M. S., Tumlinson J., O'Shea B. W., 2017, AJ, 154, 114

Pacciani L., Tavecchio F., Donnarumma I., Stamerra A., Carrasco L., Recillas E., Porras A., Uemura M., 2014, ApJ, 790, 45

Paliya V. S., Zhang H., Böttcher M., Ajello M., Domínguez A., Joshi M., Hartmann D., Stalin C. S., 2018, ApJ, 863, 98

Paliya V. S., Domínguez A., Ajello M., Olmo-García A., Hartmann D., 2021, ApJS, 253, 46

Pâris I. et al., 2018, A&A, 613, A51

Patel S. R., 2021, Proc. Sci., 37th International Cosmic Ray Conference (ICRC2021). Sissa, Trieste, PoS#824

Paturel G., Dubois P., Petit C., Woelfel F., 2002, LEDA

Predehl P., Schmitt J. H. M. M., 1995, A&A, 293, 889

Principe G., Malyshev D., Ballet J., Funk S., 2018, A&A, 618, A22

Principe G., Di Venere L., Orienti M., Migliori G., D'Ammando F., Mazziotta M. N., Giroletti M., 2021, MNRAS, 507, 4564

Raiteri C. M., Villata M., Capetti A., Heidt J., Arnaboldi M., Magazzù A., 2007, A&A, 464, 871

Raiteri C. M. et al., 2017, Nature, 552, 24623

Rolke W. A., López A. M., Conrad J., 2005, Nucl. Instrum. Methods Phys. Res. A, 551, 493

Roming P. W. A. et al., 2005, Space Sci. Rev., 120, 95

Sahakyan N., 2020, A&A, 635, A25

Saldana-Lopez A., Domínguez A., Pérez-González P. G., Finke J., Ajello M., Primack J. R., Paliya V. S., Desai A., 2021, MNRAS, 507, 5144

Schlafly E. F., Finkbeiner D. P., 2011, ApJ, 737, 103

Schmidt M., 1965, ApJ, 141, 1295

Schmuckermaier F. et al., 2023, A&A, 673, A2

Schneider D. P. et al., 2010, AJ, 139, 2360

Shaw M. S. et al., 2012, ApJ, 748, 49

Spinrad H., Smith H. E., 1975, ApJ, 201, 275

Spiridonova O. I., Vlasyuk V. V., Moskvitin A. S., Bychkova V. S., 2015, Astron. Telegram, 7004

Takalo L. O., Nilsson K., Lindfors E., Sillanpää A., Berdyugin A., Pasanen M., 2008, AIP Conf. Proc. Vol. 1085, Proceedings of the 4th International Meeting on High Energy Gamma-Ray Astronomy. Am. Inst. Phys., New York, p. 705

Urry C. M., Padovani P., 1995, PASP, 107, 803

van den Berg J. P., Böttcher M., Domínguez A., López-Moya M., 2019, ApJ, 874, 47

Villata M. et al., 2006, A&A, 453, 817

Vlasyuk V. V., Spiridonova O. I., Moskvitin A. S., Bychkova V. S., 2015, Astron. Telegram, 6970

Vlasyuk V. V., Moskvitin A. S., Spiridonova O. I., Bychkova V. S., 2018, Astron. Telegram, 12111

Wagner S., Rani B., H. E. S. S. Collaboration, 2021, Astron. Telegram, 15020

Wakely S. P., Horan D., 2008, Proc. Sci., 30th International Cosmic Ray Conference (ICRC07). Sissa, Trieste, PoS#1341

Wendel C., Shukla A., Mannheim K., 2021, ApJ, 917, 32

Wood M., Caputo R., Charles E., Di Mauro M., Magill J., Perkins J. S., Fermi-LAT Collaboration, 2017, Proc. Sci., Vol. 301, 35th International Cosmic Ray Conference (ICRC2017). Sissa, Trieste, PoS#824

Xiong D. R., Zhang X., 2014, MNRAS, 441, 3375

Zacharias M., 2018, Heas. Conf. 33

Zacharias M. et al., 2019, Galaxies, 7, 41

Zacharias M. et al., 2021, Proc. Sci., Vol. 301, 35th Int. Cosmic Ray Conf. (ICRC2017). Sissa, Trieste, PoS#655

Zanin R. et al., 2013, Proc. Sci., Vol. 33, International Cosmic Ray Conference. Sissa, Trieste, PoS#2937

APPENDIX A: LIGHT CURVES OF THE REMAINING SOURCES

In this part of the paper, we present plots that are not included in the main text of the paper.

A1 Light curves of all sources
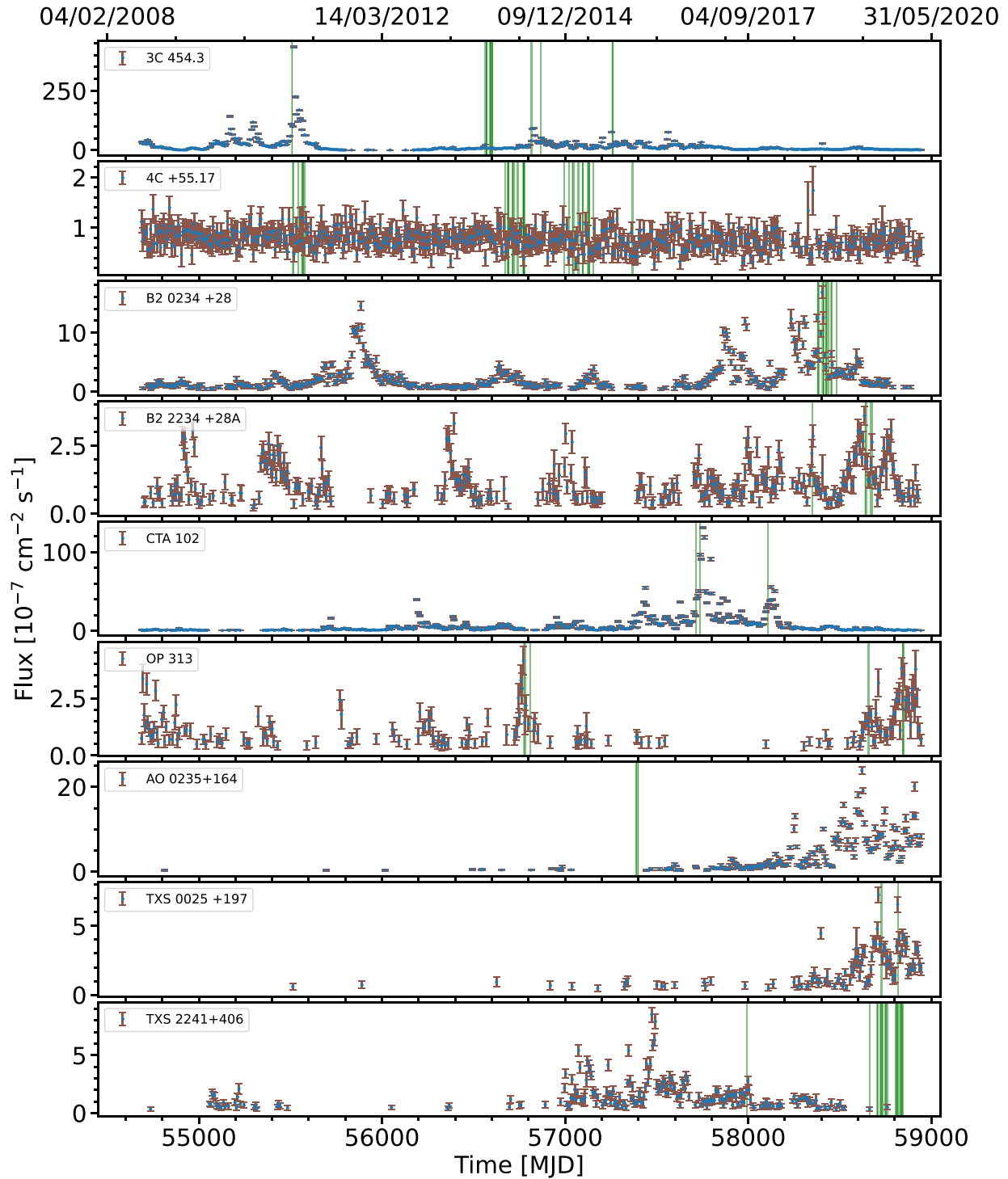
Figure A1. Fermi-LAT light curve representing the flux from 2008 to 2020. For clarirty, only flux values (with TS > 10) are shown in the plot, ULs are not reported. The vertical areas on the graph indicate the specific days when MAGIC observations were carried out. This data are presented in weekly bins with an energy range of 0.1–1000 GeV.
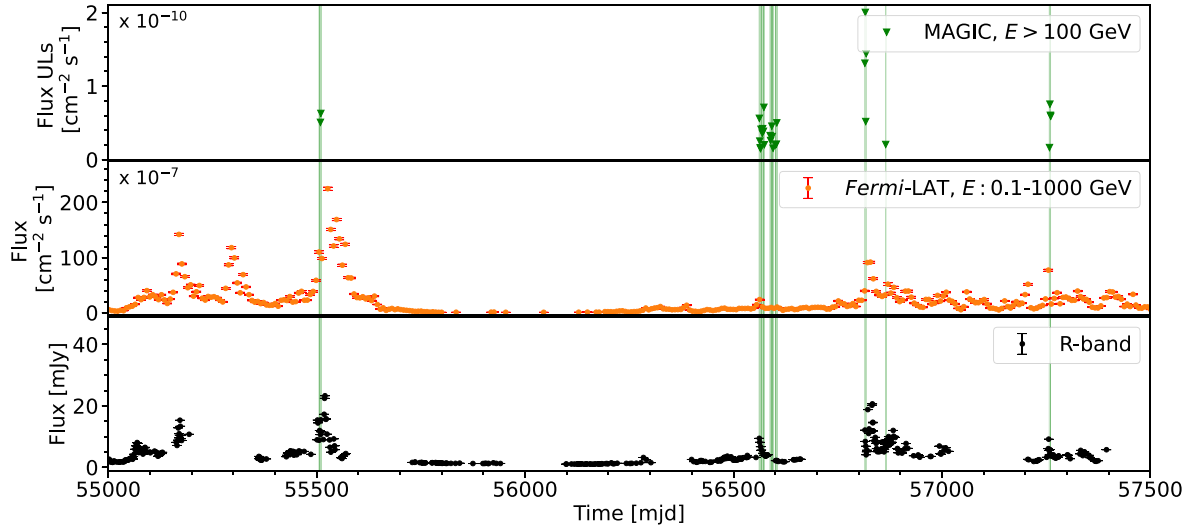
Figure A2. MWL light curve of 3C 454.3. It shows the observations carried by MAGIC (top panel), Fermi-LAT (middle panel), and the *R* band of *Swift*-UVOT (bottom panel). The vertical areas indicate the days during which MAGIC observations were carried out. Fermi-LAT light curve is presented in weekly bins and for the energy range of 0.1–1000 GeV. For clarirty, only Fermi-LAT flux values (with TS > 10) are shown in the plot, ULs are not reported.
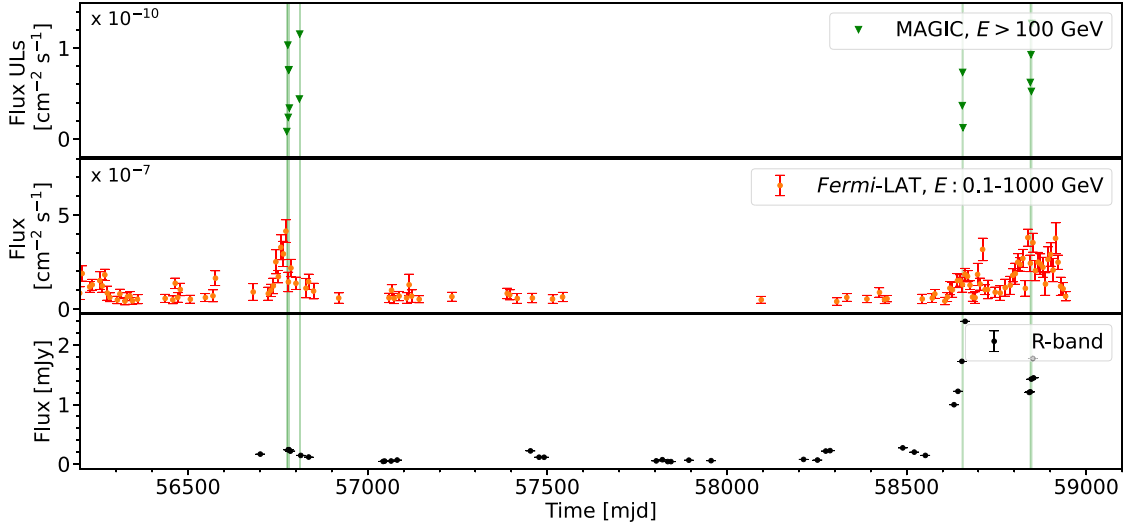
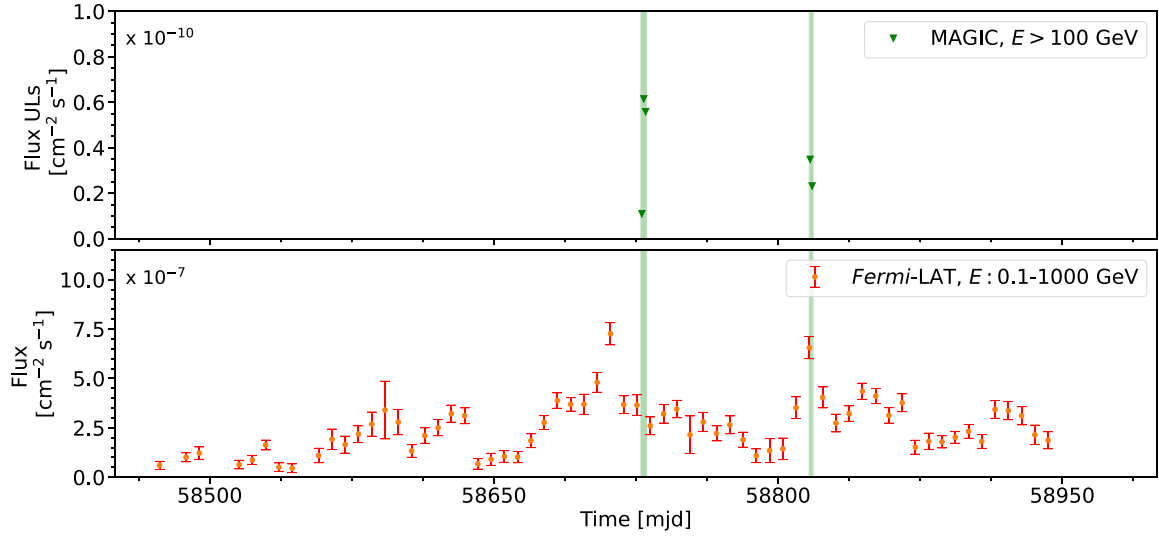**Figure A3.** MWL light curve of OP 313. The labels are the same as Fig. A2.

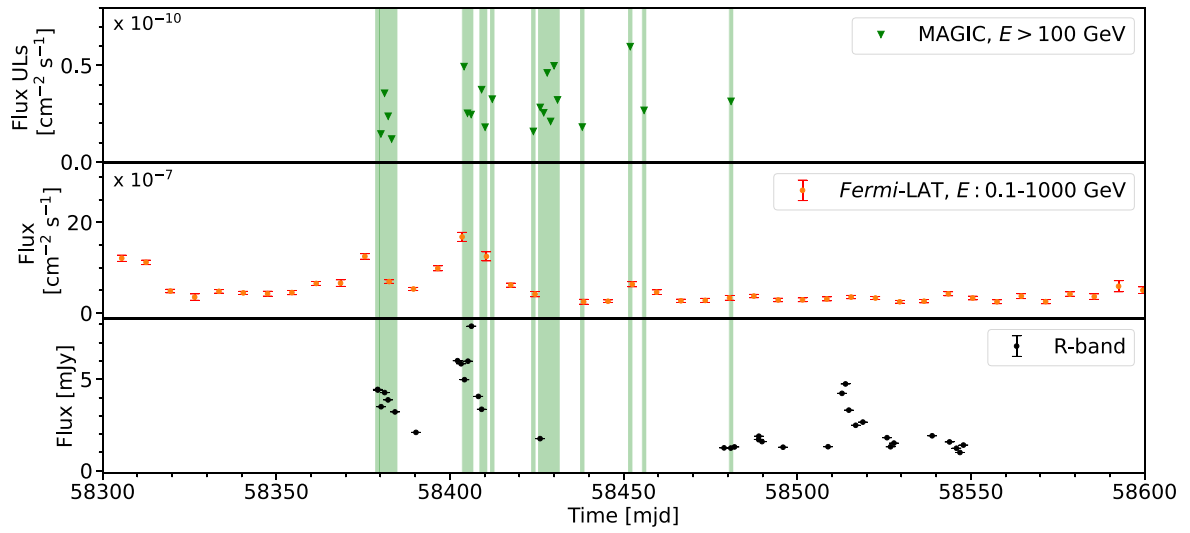**Figure A4.** MWL light curve of TXS 0025+197. The labels are the same as Fig. A2.
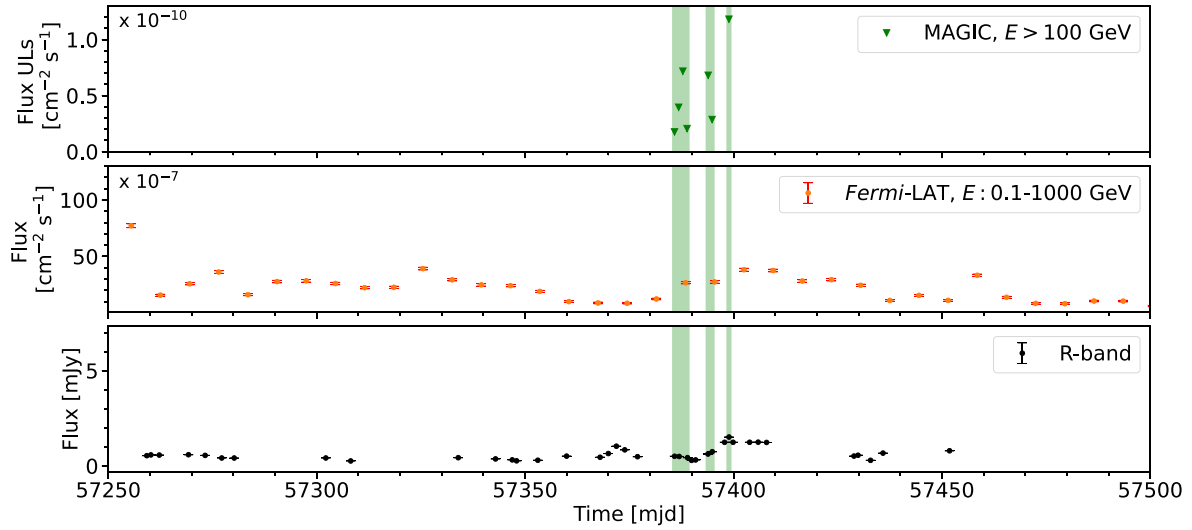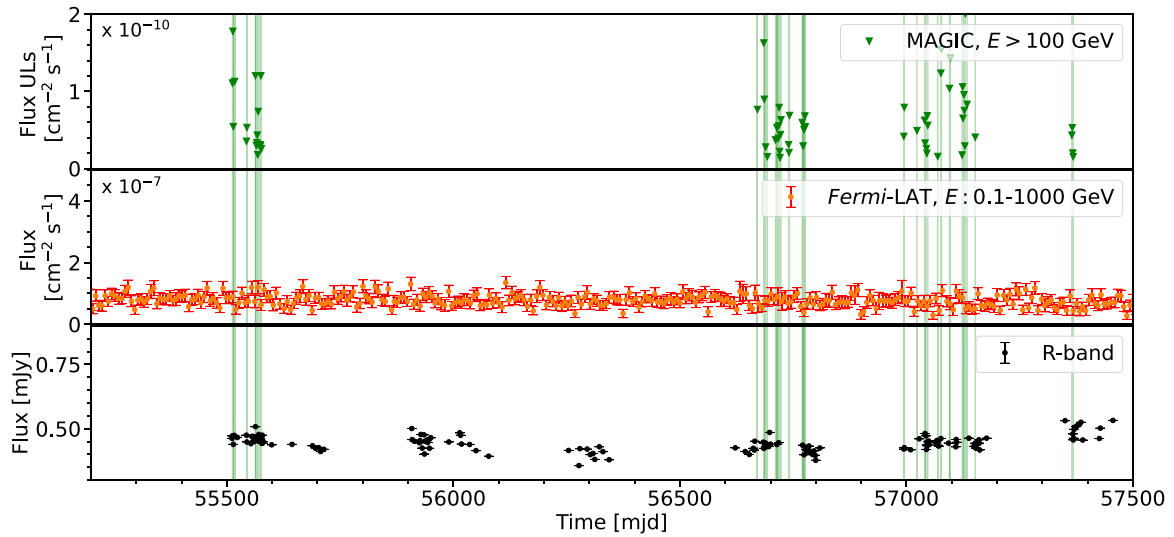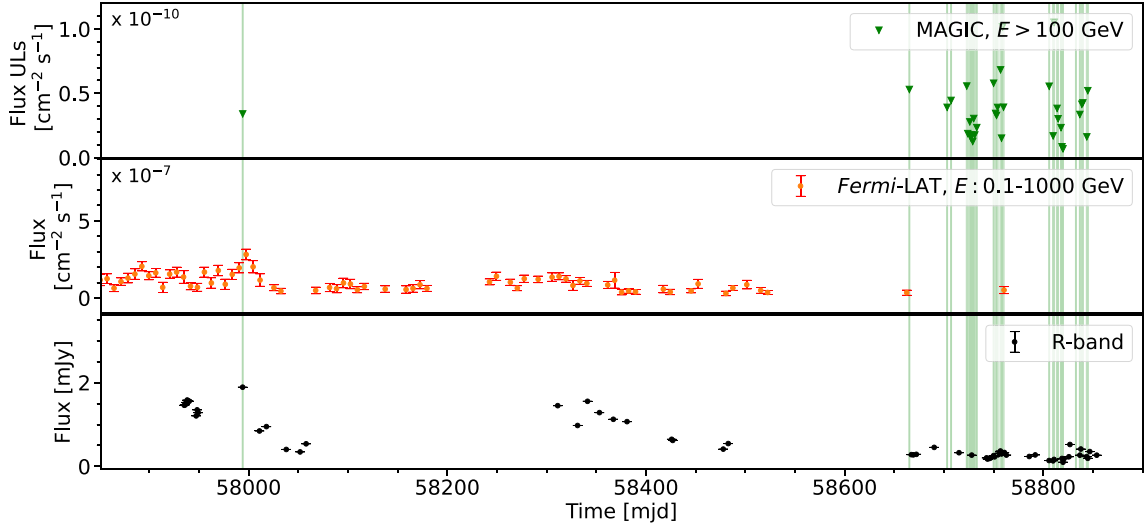

Figure A5. MWL light curve of B2 0234+28. The labels are the same as Fig. A2.

Figure A6. MWL light curve of AO 0235+16. The labels are the same as Fig. A2.

Figure A7. MWL light curve of 4C 55.17. The labels are the same as Fig. A2.

Figure A8. MLW light curve of TXS 2241+406. The labels are the same as Fig. A2.

Table A1. Days when the MAGIC observations were carried out. These represent the time interval used for the *Fermi*-LAT analysis (see Section 2.2). The one-day intervals are centred on the MAGIC observations. If observations occurred on consecutive days, then the integrated period, from the first day of observation to the last consecutive day of observation, is reported.

Association name	MJDs - 50000
TXS 0025+197	8727.56–8730.56, 8816.40–8818.40
B2 0234+28	8378.60–8379.60, 8379.62–8384.62, 8403.56–8406.56, 8408.61–8410.61, 8411.68–8412.68, 8423.51–8424.51, 8425.49–8431.49, 8437.59–8438.59, 8451.39–8452.39, 8455.39–8456.39, 8480.43–8481.43
AO 0235+16	7385.35–7389.35, 7393.42–7395.42, 7398.40–7399.40
4C +55.17	5511.74–5514.74, 5516.73–5517.73, 5542.73–5544.73, 5562.68–5563.68, 5564.70–5569.70, 5572.68–5576.68, 6670.78–6671.78, 6684.70–6686.70, 6688.69–6689.69, 6692.57–6693.57, 6710.58–6711.58, 6713.59–6715.59, 6716.58–6723.58, 6739.47–6742.47, 6769.46–6770.46, 6771.46–6772.46, 6773.44–6774.44, 6775.44–6777.44, 6993.75–6995.75, 7022.75–7023.75, 7039.70–7041.70, 7043.71–7047.71, 7068.65–7069.65, 7075.65–7077.65, 7094.58–7095.58, 7096.59–7097.58, 7122.49–7125.49, 7126.50–7130.50, 7133.45–7134.45, 7151.43–7152.43, 7364.72–7368.72
OP 313	6774.51–6775.51, 6777.42–6782.42, 6809.47–6811.47, 8654.42–8657.42, 8843.76–8844.76, 8845.72–8848.72
CTA 102	7715.40–7717.40, 7737.33–57739.33, 7748.34–57749.34, 8105.32–8106.32
B2 2234+28A	8351.66–8352.66, 8638.69–8639.69, 8642.68–8644.68, 8667.63–8668.63, 8676.67–8677.67
TXS 2241+406	7993.56–7994.56, 8664.66–8665.66, 8702.69–8703.69, 8706.68–8707.68, 8722.48–8724.48, 8725.53–8731.53, 8732.55–8733.55, 8749.51–8750.51, 8751.50–8754.50, 8756.49–8760.49, 8805.43–8806.43, 8809.42–8811.42, 8813.41–8815.41, 8817.36–8820.36, 8832.35–8833.35, 8836.32–8837.34, 8838.34–8840.34, 8843.33–8845.33
3C 454.3	5505.47–5506.47, 5508.42–5510.42, 6561.41–6566.41, 6568.40–6570.40, 6571.38–6574.38, 6587.37–6589.37, 6591.38–6593.38, 6594.36–6595.36, 6600.35–6601.35, 6602.35–6604.35, 6814.67–6818.67, 6864.67–6865.67, 7257.60–7259.60, 7259.65–7260.65

[1]*Japanese MAGIC Group: Institute for Cosmic Ray Research (ICRR), The University of Tokyo, Kashiwa, 277-8582 Chiba, Japan*

[2]*ETH Zürich, CH-8093 Zürich, Switzerland*

[3]*Università di Siena and INFN Pisa, I-53100 Siena, Italy*

[4]*Institut de Física d'Altes Energies (IFAE), The Barcelona Institute of Science and Technology (BIST), E-08193 Bellaterra (Barcelona), Spain*

[5]*ICCUB, IEEC-UB, Universitat de Barcelona, E-08028 Barcelona, Spain*

[6]*Instituto de Astrofísica de Andalucía-CSIC, Glorieta de la Astronomía s/n, E-18008 Granada, Spain*

[7]*National Institute for Astrophysics (INAF), I-00136 Rome, Italy*

[8]*Università di Udine and INFN Trieste, I-33100 Udine, Italy*

[9]*Max-Planck-Institut für Physik, D-85748 Garching, Germany*

[10]*Università di Padova and INFN, I-35131 Padova, Italy*

[11]*Faculty of Electrical Engineering and Computing (FER), Croatian MAGIC Group: University of Zagreb, , 10000 Zagreb, Croatia*

[12]*IPARCOS Institute and EMFTEL Department, Universidad Complutense de Madrid, E-28040 Madrid, Spain*

[13]*Centro Brasileiro de Pesquisas Físicas (CBPF), 22290-180 URCA, Rio de Janeiro (RJ), Brazil*

[14]*Instituto de Astrofísica de Canarias and Dpto. de Astrofísica, Universidad de La Laguna, E-38200 La Laguna, Tenerife, Spain*

[15]*Faculty of Physics and Applied Informatics, Department of Astrophysics, University of Lodz, PL-90-236 Lodz, Poland*

[16]*Centro de Investigaciones Energéticas, Medioambientales y Tecnológicas, E-28040 Madrid, Spain*

[17]*Departament de Física, and CERES-IEEC, Universitat Autònoma de Barcelona, E-08193 Bellaterra, Spain*

[18]*Università di Pisa and INFN Pisa, I-56126 Pisa, Italy*

[19]*INFN MAGIC Group: INFN Sezione di Bari and Dipartimento Interateneo di Fisica dell'Università e del Politecnico di Bari, I-70125 Bari, Italy*

[20]*Department for Physics and Technology, University of Bergen, 5007 Bergen, Norway*

[21]*INAF – Istituto di Radioastronomia, Via Gobetti 101, I-40129 Bologna, Italy*

[22]*INFN MAGIC Group: INFN Sezione di Torino and Università degli Studi di Torino, I-10125 Torino, Italy*

[23]*INFN MAGIC Group: INFN Sezione di Catania and Dipartimento di Fisica e Astronomia, University of Catania, I-95123 Catania, Italy*

[24]*Faculty of Physics, Croatian MAGIC Group: University of Rijeka, 51000 Rijeka, Croatia*

[25]*Universität Würzburg, D-97074 Würzburg, Germany*

[26]*Technische Universität Dortmund, D-44221 Dortmund, Germany*

[27]*University of Geneva, Chemin d'Ecogia 16, CH-1290 Versoix, Switzerland*

[28]*Japanese MAGIC Group: Physics Program, Graduate School of Advanced Science and Engineering, Hiroshima University, 739-8526 Hiroshima, Japan*

[29]*Deutsches Elektronen-Synchrotron (DESY), D-15738 Zeuthen, Germany*

[30]*Armenian MAGIC Group: ICRANet-Armenia, 0019 Yerevan, Armenia*

[31]*Faculty of Electrical Engineering, Mechanical Engineering and Naval Architecture (FESB), Croatian MAGIC Group: University of Split, 21000 Split, Croatia*

[32]*Department of Physics, Croatian MAGIC Group: Josip Juraj Strossmayer University of Osijek, 31000 Osijek, Croatia*

[33]*Finnish MAGIC Group: Finnish Centre for Astronomy with ESO, Department of Physics and Astronomy, University of Turku, FI-20014 Turku, Finland*

[34]*Japanese MAGIC Group: Department of Physics, Tokai University, Hiratsuka, 259-1292 Kanagawa, Japan*

[35]*Saha Institute of Nuclear Physics, A CI of Homi Bhabha National Institute, Kolkata 700064, West Bengal, India*

[36]*Inst. for Nucl. Research and Nucl. Energy, Bulgarian Academy of Sciences, BG-1784 Sofia, Bulgaria*

[37]*Max-Planck-Institut für Physik, D-85748 Garching, Germany*

[38]*Japanese MAGIC Group: Department of Physics, Yamagata University, Yamagata 990-8560, Japan*

[39]*Finnish MAGIC Group: Space Physics and Astronomy Research Unit, University of Oulu, FI-90014 Oulu, Finland*

[40]*Japanese MAGIC Group: Chiba University, ICEHAP, 263-8522 Chiba, Japan*

[41]*Japanese MAGIC Group: Institute for Space-Earth Environmental Research and Kobayashi–Maskawa Institute for the Origin of Particles and the Universe, Nagoya University, 464-6801 Nagoya, Japan*

[42]*Japanese MAGIC Group: Department of Physics, Kyoto University, 606-8502 Kyoto, Japan*

[43]*INFN MAGIC Group: INFN Roma Tor Vergata, I-00133 Roma, Italy*

[44]*Japanese MAGIC Group: Department of Physics, Konan University, Kobe, Hyogo 658-8501, Japan*

[45]*Space Science Data Center – Agenzia Spaziale Italiana, Via del Politecnico, snc, I-00133 Roma, Italy*

This paper has been typeset from a TEX/LATEX file prepared by the author.